Available online at www.sciencedirect.com

SciVerse ScienceDirect

Procedia Engineering 00 (2012) 000–000

Procedia Engineering

www.elsevier.com/locate/procedia

5th BSME International Conference on Thermal Engineering

Aerodynamics of Tip Leakage Flows Near Partial Squealer Rims in an Axial Flow Turbine

Narendra Bansode and M. Govardhan

Department of Mechanical Engineering, I.I.T. Madras, Chennai 600 036, India

Abstract

The objective of present investigation is to study aerodynamics of tip leakage flows near partial squealer rims in an axial flow turbine. Objectives are met by studying (a) tip leakage flows in clearance case with clearance of 2% of chord (2.04 mm) between blade tip and end wall without squealer rims and (b) with different squealer rim geometries to find out optimum squealer rim for a given domain. Squealer rims were incorporated on the suction and pressure surfaces either partially or fully and for each case the losses were estimated. The coefficient of secondary loss coefficient (CSKE) is used as objective function. Minimum CSKE indicates minimum losses. Squealer rim on blade suction surface reduced tip leakage losses as compared to case without squealer rim. Reduced deviation of exit flow angle due to presence of squealer rim increased higher energy transfer between blade and flow. From the investigations it is concluded that full suction side squealer rim is the optimum squealer geometry among all cases studied.

***Keywords*:** Squealer rim; tip clearance; optimum geometry; coefficient of secondary kinetic energy

Nomenclature

a	axial chord (m)
C	velocity (m/s)
C_m	meridional velocity (m/s)
C_p	static pressure coefficient
C_u	tangential velocity (m/s)
h	blade height (m)
P	pressure (N/m^2)
x	distance in the axial direction (m)
z	distance in the spanwise direction(m)
Greek symbols	
α	flow angle (deg.)
ρ	density (kg/m^3)
δ	boundary layer thicknesses(m)
Subscripts	
2	*outlet*
atm	*atmospheric*
sec	secondary

* Corresponding author. Tel.: +91-44-22574659; fax: +91-44-22574659.
E-mail address: gova@iitm.ac.in

1.0 Introduction

Squealer tips or rims are projections over the turbine blade end surface. They reduce gap between blade and the end wall protect the blade tip from the full impact of high temperature leakage gases. The additional advantage of these squealer tip geometries is that, these geometries also reduce tip leakage losses. Squealer rims can be employed on full blade surface or partially on the suction surface or the pressure surface. Different positions and lengths of rims also affect the flow behavior (Metzger et al. [1] and Chyu et al. [2]). Metzger et al. [1]concluded that for a given pressure difference across the gap there is an optimum value of depth to width ratio beyond which no further flow reduction will occur. Heyes *et al.* [3] indicated in their studies that suction side squealer configuration provided the greatest gains in terms of eliminating leakage flow losses. Another advantage of squealer tip geometries is that they provide an overall lower heat transfer coefficient compared to flat tip geometry (Azad et al. [4].

Dey *et. al.* [5] studied experimental investigation of aerodynamic characteristics of full and partial-length squealer rims in a turbine stage. Their results also show that the suction side partial squealers are aerodynamically superior to the pressure side squealers and the channel arrangement. The numerical results of Camci et al. [6] also showed that the suction side partial squealer rims are capable of reducing the aerodynamic losses associated with the leakage flow to a significant degree. A comparison of the numerically visualized tip gap flow field and measured aerodynamic field in the turbine suggests that simulations are effective in explaining local three dimensional flow details in turbine flow zones in which aerodynamic measurements are difficult to perform. Kavurmacioglu et al. [7] demonstrated that partial squealer rim arrangement can be extremely effective in weakening the tip leakage vortex in a turbine tip leakage vortex. The study also showed that the chord-wise length of partial squealer rim near the suction side corner does not significantly effect the desensitization process. Camci et al. [8] found that the suction side partial squealers are aerodynamically superior to pressure side ones and channel arrangement and are capable of reducing the stage exit total pressure defect associated with the tip leakage flow to a significant degree. Key and Arts [9] compared plane tip leakage flow with squealer tip one at high speed conditions and showed that the squealer tip provides a significant decrease in velocity through the tip gap. Lee and Chae [10] in their investigations on high turning turbine rotor blades reported that the tip leakage vortex tends to become weak and the interaction between the tip leakage vortex and the passage vortex became less severe with the increase in squealer rim height to chord ratio

2. Computational Methodology

Numerical investigations were conducted on a reaction turbine blade cascade with a blade deflection of 100^0). Grid is made in ICEM-CFD. Hexahedral mesh is employed for the domain and around the blade O-grid is made to get highly orthogonal grid for accurate solutions. Near the blade, cell height of 0.01 mm (first cell height normal to surface) is used and contains 30 layers in a distance of 3 mm normal to wall. For end wall surface, cell height of 0.004 mm (for first cell height and ratio is 1.05 for consequent cells) is used. In clearance case, clearance of 2.04 mm is uniformly divided into 80 numbers of layers. For squealer surfaces same grid is employed as that for the blade. Skewness of the grid is 0.26 and quality of grid is above 0.3 which is considered as good to yield correct results. Y+ for all solid surfaces is below 2. CFD code used for the investigation in this study is the general-purpose code ANSYS CFX 13.0, and is based on a node centered finite-volume approach.

According to method of characteristics, flow angle, total pressure, total temperature and isentropic relations are used as boundary condition at the subsonic axial inlet. Working fluid is incompressible air, as the inlet Mach number is very low. All solid walls are set with no slip condition and adiabatic. At inlet experimentally measured total pressure profile for 0° incidence is specified with a turbulence intensity of 1 % and integral length scale of 5 mm. Measured inlet boundary layer thickness (δ) is 40 mm. The baldes had a chord of 102 mm with an inlet and outlet angles of 22^0 and 60^0 respectively. The stagger angle is 30^0 and the aspect ratio is 3.9, With the blade height of 400 mm, the space-chord ratio was maintained at 0.69. Typical computational domains with details of cascade are shown in Fig. 1.

In present investigation the experimental results of Maharia [11] for no fence case are validated. All the measurements in experiments as well as in computations are taken at x/a = 1.06 where *x* is axial distance and *a* is the blade axial chord. Computational results of velocity and its three components are plotted against blade span and compared with the experimental results, (Fig. 2). The velocity ratios predicted by CFD are in excellent agreement with the measurements. After conducting grid independence study grid with 2.2 million cells is used for zero clearance case and grid with 4.4 million cells is used for case 1. The geometry along with squealer tip geometries for all cases are shown in Fig.3.

3 Results and Discussion

The objective of current investigation is to reduce the tip leakage losses using squealer rim geometries. For this purpose a clearance gap of 2% of chord is created at between blade tip and end wall. This value (2% of chord) is chosen based on standard industrial practices. This is chosen as base case. Physical tip gap equal to 2% of chord is 2.04 mm. Thus span is 202.04 mm for case 1 including 2.04 mm of tip gap. The non-dimensionalised distance for case 1 varies from 0 to 0.505. Total seven cases, as given in Table 1, have been investigated and the results are compared with base case.

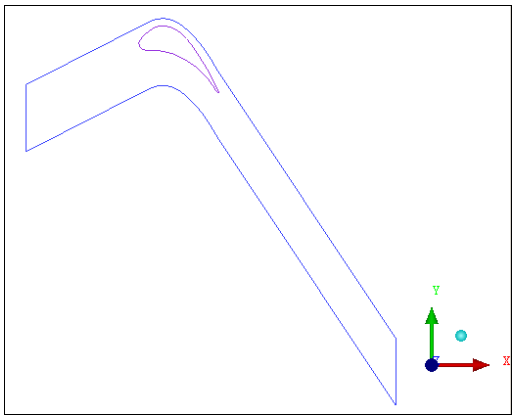

Fig.1 Computational domain with boundaries

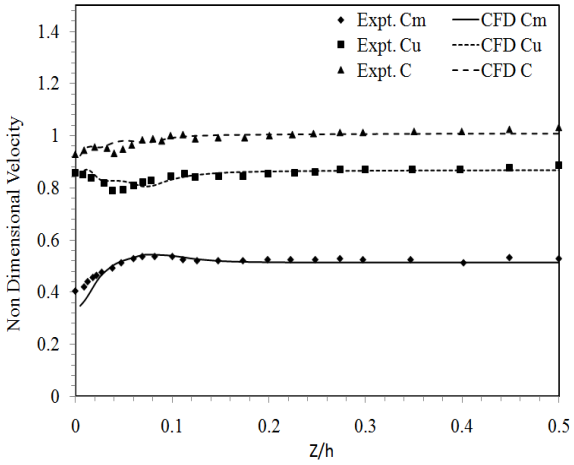

Fig.2 Validation of CFD results with experiments

3.1 Partial squealer rims

Tip clearance gap between rotating turbine blade and stationary casing is unavoidable. Due to pressure difference across the blade, flow leaks from pressure surface to suction surface and mixes with through flow. Compressor blades are usually slender and have smaller blade thickness whereas turbine blades are thicker. The pressure difference across the blade varies from leading edge to trailing edge. In the zones where the difference is maximum, leakage flow also will be maximum. Though the pressure difference across the blade (blade loading) is desirable as it is proportional to the lift force, it is not so desirable near the tip of the blade. In compressor blades, the flow from end wall as well as from blade tip surface emerge from suction surface of the blade as the two jets of two streams and roll into tip leakage vortex in the passage. This vortex obviously modifies the flow structure near to the end wall. The passage vortex is pushed down. On the other hand in turbine blades, the flow from end wall and blade tip surface mix out in the tip gap itself creating mixing losses within the tip gap. The clearance vortex is formed within the gap itself, grows and emerges from the suction surface. Hence in order to decide the length and position of the partial squealer rim geometries, static pressure coefficient (Cp) variation along blade suction and pressure surfaces is plotted just below the blade tip (2% from the blade tip or at 98% of the span from hub) for suction side squealer rim and pressure side squealer rim. This Cp variation is compared to that of without squealer rim as shown in Figs. 4(a0 and 4(b). These graphs throw light on the position and length of squealer rim geometries. The height of the squealer rim geometry is maintained at 1.02 mm (half of the tip gap) and width of the squealer rim is 5 mm (18 % of blade thickness of the blade). Cp is defined as

$$C_p = \frac{P - P_{atm}}{\frac{\rho}{2}\bar{\bar{C}}_2^2} \quad (1)$$

Where $\bar{\bar{C}}_2^2$ is pitchwise and spanwise mass averaged exit velocity at x/a=1.06 and P is static pressure at any point on the blade surface.

Fig. 4(a) shows the static pressure distribution along the blade surface with squealer rim placed on full suction side. The suction side squealer rim has considerable effect on the pressure distribution along the blade surface. The reduction in static pressure is good for certain chord length. Static pressure with squealer rim is high from the leading edge to x/a = 0.68 compared to the case without rim. The increased static pressure up to x/a = 0.68 indicates that the blade loading is reduced with a consequent reduction in the leakage flow. Cp distribution in Fig. 4(b) shows that squealer rim on full pressure side does not have much effect on pressure distribution on suction side. It has little effect on the pressure side. From these

observations total of six different squealer rim geometries are created and computationally simulated. The results obtained are compared with that obtained from without squealer rim geometry (Case 1). All these seven cases are already listed in Table 1.

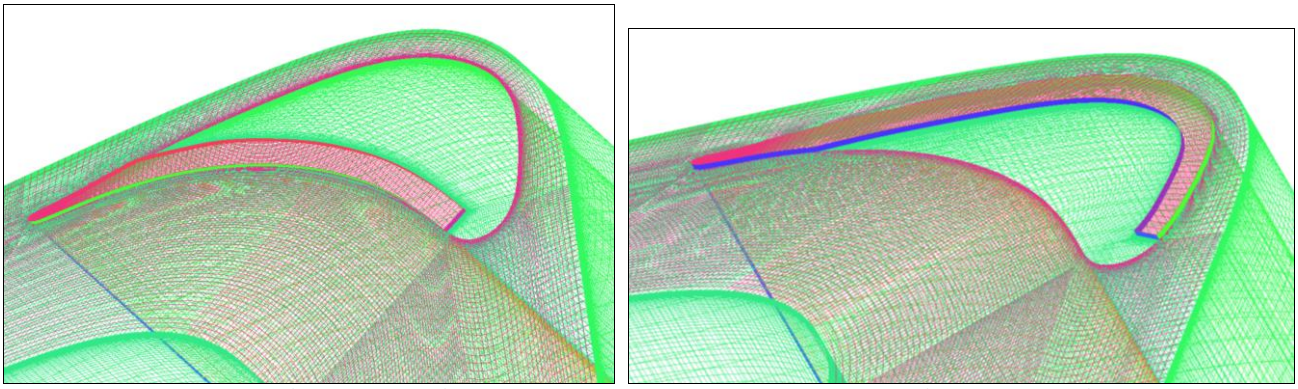

Case 1 Squealer rim on full suction side of blade

Case 2 Squealer rim on full pressure side of blade

Figure 3 Detail view of mesh along with squealer tip configuration

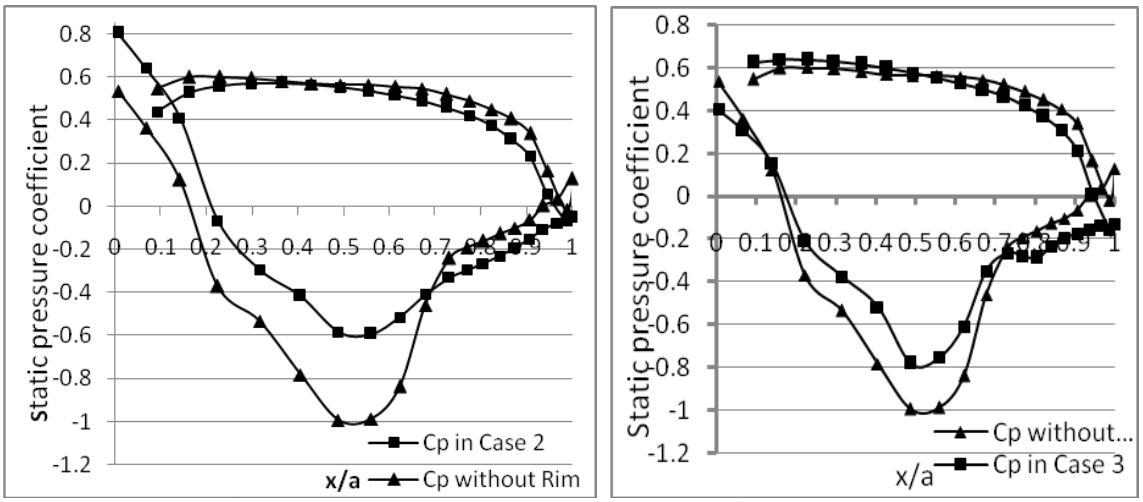

(a) full suction side squealer rim

(b) full pressure side squealer rim

Fig. 4 Static pressure coefficien distribution from LE to TE at 99% of blade height with full suction side squealer rim

3.2 Results with partial squealer rims

As the total pressure loss coefficient from CFD analysis not entirely reliable, CSKE is used as objective function. Reduction in CSKE is indication of reduction in total losses. CSKE is defined as follows

$$\text{SKE} = \frac{1}{2}\rho(c_{\text{sec}}^2 + c_r^2) \tag{2}$$

Where SKE is secondary kinetic energy and

$$c_{\text{sec}} = -c_m \sin\bar{\bar{\alpha}}_2 + c_u \cos\bar{\bar{\alpha}}_2 \quad \text{and} \quad \text{CSKE} = \frac{SKE}{\frac{1}{2}\rho \bar{\bar{c}}_2^2} \tag{3}$$

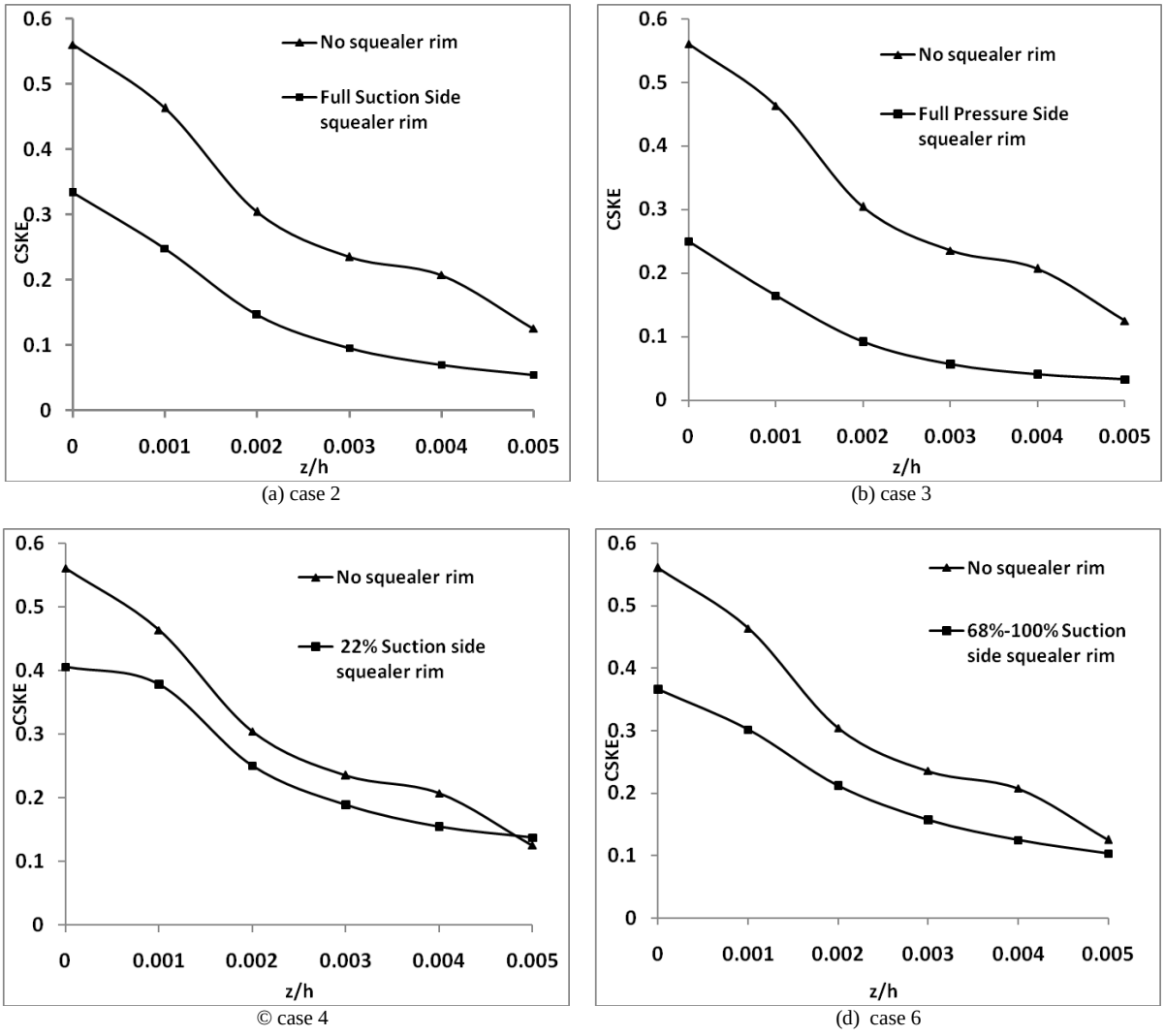

(a) case 2 (b) case 3

© case 4 (d) case 6

Fig. 5 Spanwise variation of pitchwise mass averaged CSKE in cleaance gap

Figures 5(a) – 5(d) show spanwise variation of pitchwise mass averaged CSKE for cases 2, 3, 4, 6, respectively in clearance gap alone, plotted at x/a=1.06. Every case shows reduction in CSKE value in clearance gap as compared with case 1 (no squealer rim). Cases 2, 3 and 6 show considerable reductions in CSKE while in cases 4, 5 and 7 CSKE reduction is moderate. This is because in cases 2 and 3 squealer rim is along full suction side and full pressure side respectively and hence flow passing through clearance between blade tip and end wall is effectively blocked. In case 6, squealer rim is placed on the suction side of blade tip from 68 % to 100% of axial chord. Thus it is capable of blocking of tip leakage vortex which otherwise emerge into the passage. In cases 4, 5 and 7 squealer rims are not that much effective in blocking the tip clearance flow. (for cases 5 and 7 refer Table 1).

The exit blade angle is 60^0 and ideally flow should follow the blade angle. But due to presence gradients and relative circulation within the blade passage, flow deviation occurs and hence the flow angle is always less than the blade angle. Fig. 6 shows spanwise variation of pitchwise mass averaged exit flow angle for different squealer rim geometry cases in clearance alone. We can see that employment of squealer rim reduces flow deviation, but not very effectively in the clearance. From Table 1 it can observed that exit flow angle is increased for cases 2, 5, 6 and 7 as compared to that of case 1, hence deviation is less in these cases. For cases 3 and 4 exit flow angle is reduced compared to case 1.

Mass averaged CSKE values and exit flow angle for all seven cases are calculated for complete span and clearance alone on the outlet plane located at x/a = 1.06 and are listed in Table 1.CSKE is least for case 2. Thus out of seven cases studied the squealer rim on full suction side of blade (case 2) is considered as optimum squealer rim.

3.3 Wall shear along with velocity streamlines

Wall shear contours along with velocity streamlines are plotted on end wall shown in Figs. 7(a) and 8(b). Velocity streamlines describe the flow immediately on the surface of the body. In two dimensional flows boundary layer separation is characterised by means of a reverse flow or vanishing wall shear stress, but in case of a three dimensional flow vanishing wall shear stress is not the bounding criterion. In three dimensional separations, wall shear may have value other than zero. A necessary condition for the occurrence of flow separation in three dimensions is the convergence of streamlines onto a separation line. In Fig. 8(a) saddle point can be seen just in front of blade tip, it is also a critical point. Point of separation and point of reattachment are critical points and hence value of wall shear is also zero. The streamline on which other streamlines are converging is a separation line. It is formed due to lift off horseshoe vortex and passage vortex. These separation lines are the footprint of these vortices. In squealer rim cases saddle point is either vanished or reduced and wall shear is not zero near front of blade tip.

3.4 Total pressure loss coefficient contours

Figs. 8(a) and 8(b) show total pressure loss coefficient contours on the end wall. The total pressure losses are significantly higher near the blade surface. Total pressure loss coefficient is reduced significantly compared to case 1.

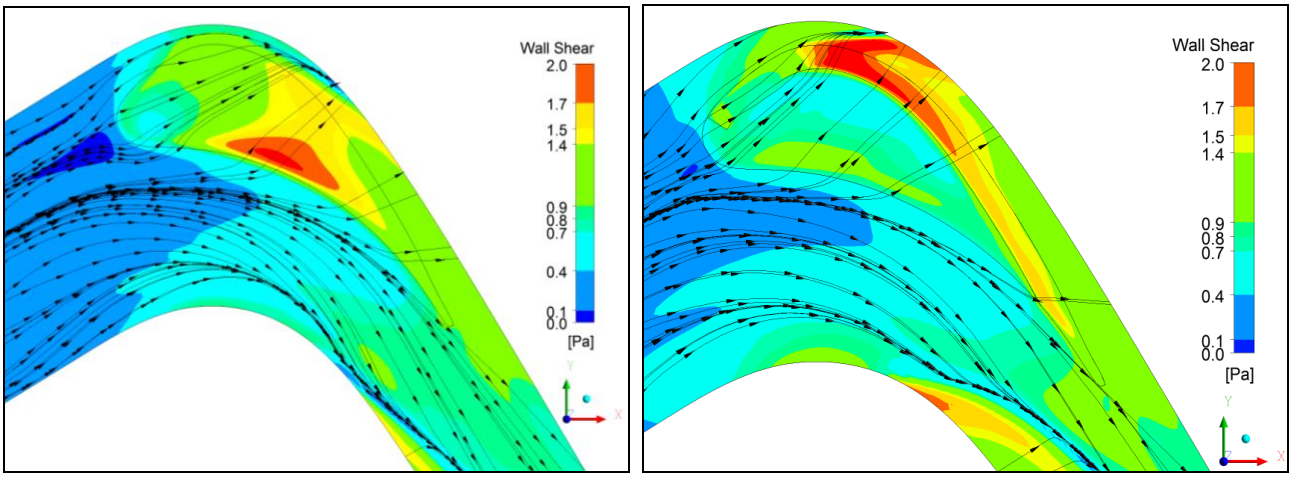

case 1 case 2

Fig. 6 Wall shear along with velocity streamlines on the end wall

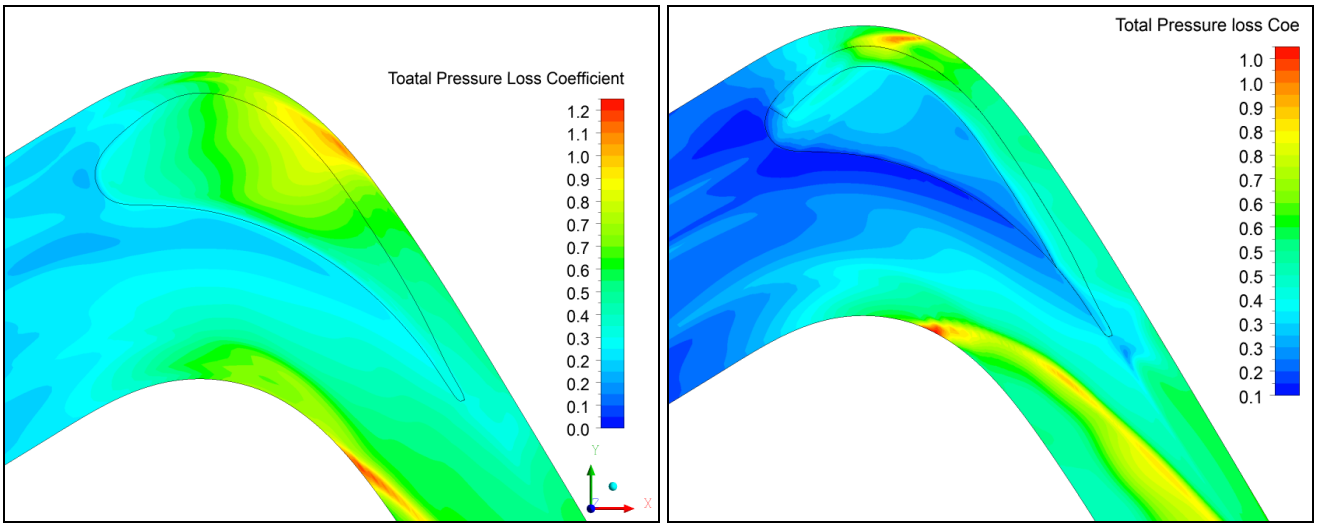

case 1 case 2

Fig. 7 Total pressure loss coefficient contours on the end wall

4. Conclusions

The objective of this project was to study the effect of partial squealer rim on tip leakage flow which was accomplished by simulating the single passage of turbine cascade. Squealer rim on blade surface reduces CSKE and hence reduces tip leakage losses as compared to no squealer rim. Due to presence of squealer rims flow deviation is reduced. Reduced deviation of exit flow angle indicates higher energy transfer between blade and flow. Suction side squealer rims are capable of reducing the tip leakage losses than the pressure side squealer rims. The optimum squealer rim is one which is placed along full suction surface on the blade tip. It has least SKE and hence produces least tip leakage losses. CSKE reduction up to 39% is achieved by optimum squealer rim. It is capable of blocking of tip leakage vortex which otherwise emerge into the passage.

Table 1. Mass averaged CSKE and exit flow angle at x/a = 1.06

No	Case	Name of Case	CSKE (m/s)		Exit Flow Angle (degree)	
			Complete span	Clearance gap alone	Complete span	Clearance gap alone
1	Case 1	Without squealer rim	8.40E-03	2.43E-01	57.54	31.07
2	Case 2	Squealer rim on full suction side of blade	3.25E-03	1.65E-01	58.39	29.85
3	Case 3	Squealer rim on full pressure side of blade	6.11E-03	1.03E-01	56.76	40.76
4	Case 4	Squealer rim till 22% of axial chord on suction side of blade	8.37E-03	2.62E-01	56.76	29.75
5	Case 5	Squealer rim till 68% of axial chord on suction side of blade	6.31E-03	3.01E-01	58.03	29.00
6	Case 6	Squealer rim on suction side of blade from 68% to 100% of axial chord	6.33E-03	2.17E-01	57.78	30.37
7	Case 7	Squealer rim on suction side of blade from 22% to 68% of axial chord	6.24E-03	2.91E-01	57.86	29.61

References

[1] Metzger, D.E., Bunker, R.S. and Chyu, M.K., 1989. Cavity Heat Transfer on a Transverse Grooved Wall in a Narrow Channel. Journal of Heat Transfer 111, p.73.

[2] Chyu, M.K., Moon, H.K. and Metzger, D.E., 1989 Heat Transfer in the Tip Region of Grooved Turbine Blades. ASME Journal of Turbomachinery 111, p.131.

[3] Heyes, F.J.G., Hodson, H.P. and Dailey, G.M., 1992 The Effect of Blade Tip Geometry on the Tip Leakage Flow in Axial Turbine Cascades. ASME Journal of Turbomachinery 114, p.643.

[4] Azad, G.M.S., Han, J.C and Boyle, R.J., 2000. "Heat Transfer and Flow on the Squealer Tip of a Gas Turbine Blade". ASME paper 2000-GT-195.

[5] Dey, D., Camci, C. and Kavurmacioglu, L., 2003. "Tip Leakage Flows Near Partial Squealer Rims in an Axial Flow Turbine Stage," ASME IGTI Turbo Expo Atlanta, Georgia, paper GT2003-38979.

[6] Camci, C., Dey, D. and Kavurmacioglu, L., 2004. "Tip Leakage Flows Near Partial Squealer Rims in an Axial Flow Turbine Stage". von Karman Institute Lecture Series VKI-LS 2004-02, "Turbine Blade Tip Design and Tip Clearance Treatment," Brussels, pp. 85-101.

[7] Kavurmacioglu L Dey D and Camci C., 2007. Aerodynamic Character of Partial Squealer Tip Arrangement in an Axial Flow Turbine part II. Detailed Numerical Aerodynamic Field Visualizations via Three Dimensional Viscous Flow Simulations Around a Partial Squealer Tip. Progress in Computational Fluid Dynamics 7, p. 374

[8] Camci, C., Dey, D. and Kavurmacioglu, L., 2005. Aerodynamic of Tip Leakage Flows Near Partial Squealer Rims in an Axial Flow Turbine Stage. ASME, Journal of Turbomachinery 127, p.14.

[9] Key, N. and Arts, T., 2006 Comparison of Turbine Tip Leakage Flow for Flat Tip and Squealer Tip Geometries at High Speed Conditions. ASME, Journal of Turbomachinery 128, p.213.

[10] Lee, S.W. and Chae, B.J. 2008. Effect of Squealer Rim Height on Aerodynamic Losses Downstream of a High Turning Turbine Rotor Blade. Journal of Experimental Thermal and Fluid Science 32, p.1440.

[11] Govardhan, M., and Pramod Kumar Maharia. 2010. "Secondary Loss Reduction by Streamwise Fences in a Reaction Turbine Cascade," 7th Jordanian International Mechanical Engineering Conference (JIMEC'7), Amman-Jordan, pp. 27-29.

5th BSME International Conference on Thermal Engineering

Numerical Investigation of Pressure Loss Mechanism and Cross Flow Behaviour in a Serpentine Separator and Gas Diffusion Layer of Polymer Electrolyte Membrane Fuel Cell

K. M. Salahuddin[1,*], Akira Nishimura[2], Litan Kumar Saha[3], Nobuyuki Oshima[1]

[1]*Graduate School of Engineering, Hokkaido University, Japan*

[2]*Graduate School of Engineering, Mie University, Japan*

[3]*Department of Mathematics, University of Dhaka, Dhaka-1000, Bangladesh*

Abstract

Polymer Electrolyte Membrane Fuel Cell (PEMFC) are considered to a promising candidate of power sources for vehicles in the next generation. PEMFC must overcome some engineering and economic obstacles to be more efficient and cheaper than other energy sources. In order to achieve this aim fuel cell design optimization must be conducted along with the improvement in the material system used for the development of PEMFC. In the present study, three dimensional, transient isothermal gas flow behaviour in a serpentine channel with porous media (so called GDL) of PEMFC has been investigated numerically. Various design of micro channel with low Reynolds number based on the channel width and flow velocity of gas has been optimized. The pressure drop and cross flow of gas is considered as the diagnostic tools in this study. In order to estimate the pressure drop accurately the precise calculation of mass conservation is necessary which is strictly maintained in our simulation. The physical properties like porosity and permeability has found significant impact on pressure drop. The effect of geometrical properties also has been investigated on pressure drop as well as cross flow. It is found that pressure drop increases with the decreasing gas channel pitch length. The reactant gas distributed from one part of the channel to another part through GDL by cross flow owing to the differential pressure between adjacent channels. The amount of cross-flow is quantified as volume mass flux through the GDL under the rib which is dominated by the thickness of gas diffusion layer, pitch length of channel and permeability. Permeability of GDL has strong effect on pressure drop and cross flow. A mechanism of pressure drop by cross flow and bend region in a serpentine channel has been identified. It is observed that the cross flow suppressed the pressure gradient in the channel while bend region improves the pressure gradient. The pressure gradient in the channel becomes higher when the cross flow in the channel is lower.

Keywords: PEMFC, Pitch length, Pressure drop, low Reynolds number, Permeability, Numerical Simulation

Nomenclature

Nomenclature

ε	: Porosity of porous media
μ	: Viscosity, $kgm^{-1}s^{-1}$
ρ	: Density, $kg\ m^{-3}$
K	: Permeability, m^2
p	: Pressure, Pa
Q	: Volume Flow rate, m^3s^{-1}
$\mathbf{u}$	: Flow velocity vector in the flow channel, ms^{-1}

1. Introduction:

Polymer electrolyte membrane (PEM) fuel cells are electrochemical device that converts chemical energy of fuel directly into electricity. This direct conversion of chemical energy into electricity has some profound impact on the maximum theoretical efficiency of electrical devices. Polymer electrolyte membrane fuel cells are promising and worthy candidates for high efficiency/low emission energy conversion devices in the mobile, stationary and portable applications sector.

PEM fuel cells used specially designed channels machined into the bipolar plates which distribute reactant gases and remove the reaction products. The most widely used gas flow channel configuration for PEM fuel cell is the serpentine channel. The gas flow channels are grooved into the bipolar plate and gas diffusion layer (GDL) placed under the channel and bipolar plate. The area where the bipolar plate is in direct contact with the GDL is known as the "land", or, "rib". Serpentine flow channel layout has relatively long flow path, hence a substantial pressure drop, consequently significant parasitic power loss associated with cathode gas supply. In the ordinary gas flow situations the reactants reach to the catalyst layer through gas diffusion. The gas diffusion layer (GDL) plays an important role to distribute the reactants to the catalyst layer by diffusion process. However, in the case of large calculation, it is thought that the differential pressure between adjoining channel increases, and that's why the supplied gas flows through the GDL owing to the differential pressure. In this process, reactant gas flows through the GDL under the rib from one part of the channel to another part of the channel is known as cross flow.

The cross leakage flow through the GDL has been investigated as direct result of the pressure difference between two channels by Kanezaki et al., 2006. The effect of cross flow on the performance of fuel cell with serpentine flow channel design with assembly compression has been investigated by Z. Shi and X. Wang, 2008. They found that the cross flow through the GDL from one channel to another channel decreases when assembly compression is considered, the performance of fuel cell especially in the high current density region also decreases. The pressure drop and flow cross-over through GDL of a PEM fuel cell flow field with serpentine channel has been investigated by Sun et al., 2006 using the trapezoidal shape of the channel cross section. Their results indicate that the trapezoidal cross-sectional shape ratio has a significant effect on the pressure variation in the flow field for both the cross-over and no cross-over cases. The effects of GDL thickness and reactant flow rate on liquid water removal has been investigated experimentally by Jiao et al. (2010). In this study they confirmed that cross flow has significant effects on water removal, even at low flow rates. Recently, their group (Bachman et al. 2012) experimentally induced cross flow in the parallel flow field and they showed that cross flow improve 24% in the current density.

Since cross flow through GDL appears due to the pressure difference between two adjacent channels, therefore, precise calculation of pressure drop is necessary in order to predict the amount of cross flow accurately. An algorithm had been developed to solve the coupling of velocity and pressure in the momentum equation with an attention of mass conservation strictly by Saha et. al 2010. The developed algorithm has been validated in the case of GDL deformation with parallel flow field (Saha et. al 2012). Recently, our group numerically predicted the amount of flow cross-over through the GDL using five multiple serpentine channel and compared the numerical solution with experimental measurement and it was found an excellent agreement which validated the accuracy of our numerical scheme (Saha and Oshima, 2012).

According to our knowledge, no studies of flow cross-over in situations considering the pitch length (Pitch length is defined as the distance between the centre of channel and centre of rib) appears to be available. Since the dependency of pitch length is very serious regarding the uniform temperature distribution. Therefore, it requires the details analysis of flow distribution considering the pitch length effect. In the present study, we designed our computational domain based on the concept of pitch length used in the experimental work for measuring the uniform in-plane temperature distribution and found an optimal pitch length of serpentine channel (Nishimura et al., 2012). Therefore, the objective is to show the dependency of geometrical parameter as well as physical parameters of GDL on cross flow and pressure drop using different pitch length (e.g. pitch length 0.5 mm, 1.0 mm, 2.5 mm) of a single serpentine channel with various thickness of GDL.

2. Numerical procedure

2.1 Physical and Mathematical Model

In order to understand the pressure loss mechanism and cross flow behaviour , we have taken three different cross-sectional area of single serpentine channel grooved into the bipolar plate and four different thickness of GDL placed under the channel and bipolar plate with wide range of GDL permeability values and porosity. Since the pitch length of gas channel has a great impact for the performance of PEM fuel cell. Figure 1 shows the example of numerical grid used for the present simulation. Dimension of the computational domain is given in Table 1. For the simplification, the following assumptions are considered (1) ideal gas mixture; (2) incompressible and laminar flow due to low Reynolds number; (3) the GDL is considered to be isotropic porous media. We examined the gas flow only. The gas flow behavior in the gas channel and GDL can be obtained by solving the equation of continuity and momentum equation. The governing equations corresponding to the various region (i) gas channel and (ii) porous media GDL are given below.

Since the equation (1) and (2) is valid for all region is used in our present simulation, therefore, there is no need to treat the interface boundary conditions separately.

Continuity equation:

$$\frac{\partial(\varepsilon\rho)}{\partial t} + \nabla \cdot (\varepsilon\rho\,\mathbf{u}) = 0 \tag{1}$$

Momentum equation:

$$\frac{\partial}{\partial t}(\varepsilon\rho\mathbf{u}) + \nabla \cdot (\varepsilon\rho\mathbf{u}) = -\varepsilon\nabla p + \nabla \cdot (\varepsilon\mu\nabla\mathbf{u}) + \varepsilon\rho\,\mathbf{g} - \frac{\varepsilon^2\mu\mathbf{u}}{K} \tag{2}$$

where $\mathbf{u}$ is the velocity vector, μ the viscosity, ρ the density, ε the porosity of the GDL and K is the permeability of the GDL. Porosity, ε is defined by the ratio of the volume occupied by the pore to the total volume of the porous media where as permeability, K is defined by the square of the effective volume to surface area ratio of the porous matrix as in Mazumder and Cole [10]. The last term of equation (2) represents the Darcy's drag force in the porous media. In the gas channel, $\varepsilon \to 1$ and $K \to \infty$, so equation (2) becomes the original Navier-Stokes equation.

2.2 Boundary conditions

No-slip boundary conditions are applied to all wall boundaries. A constant velocity is used at the inlet of the channel. Ambient pressure is applied at the outlet.

2.3 Numerical Methods

The mass and momentum conservation equations together with the boundary conditions are solved by the software Front Flow/PEFC which is a general purpose of our numerical simulator. The equations (1) and (2) with boundary conditions are discretized by finite volume method. The software Front flow/PEFC has been developed by Computational Fluid Mechanics laboratory, Hokkaido University supported by Adaptable and Seamless Technology Transfer Program through Target-driven R & D of Japan Science and Technology Agency also includes electrical field, porous media, electrochemical reaction and water transport. Euler implicit scheme has been used for time integration. The first order upwind scheme has been applied to discretize the convection terms in the governing equations. The fractional step algorithm is used to update the pressure and velocity fields from solutions of pressure Poisson equations.

Table 1: Dimension of the computational domain

Dimension	Value
Channel width, m	0.0005, 0.001, 0.025
Land width, m	0.0005, 0.001, 0.0025
Channel height, m	0.001
GDL thickness	0.0003,0.0002, 0.00017, 0.000128
Ratio of channel width and land width	1:1
Number of channel	1
Number of U turns	4

Table 2: Physical properties and operational parameters

Physical quantity	Value
GDL porosity	0.1-0.9
GDL Permeability, K(m^2)	1.76d-5-1.76d-14
Density, ρ (kg/m^3)	1.2
Viscosity, μ (kg/m s)	1.83×10^{-5}
Operational temperature (K)	333
Operational Pressure, Pa	101325
Gas flow rate, (m^3/s)	2.0d-6
Gas composition,	O_2: 21% N_2 :79%

3. Results and Discussions:

The numerical procedure described above, physical and operational parameters are listed in Table 2 were used to obtain the numerical results presented in the following section. Fig. 2 (a)-(c) shows the velocity distribution in the channel. Velocity profile of gas flow channel becomes laminar fully developed in the downstream direction in Fig 4. The maximum velocity found at the centre of channel. As the flow approaches to turning region the symmetric velocity profile becomes asymmetric and it remains until the flow leaves the turning region. A recirculation zone can be seen around the corner of the U-turn. This zone contributes to higher friction, leading to pressure drop around the bend region. Further downstream to the turning region velocity profile becomes fully developed again and remains until flow of reactant gas comes to nearer to the next bend region. The pressure distribution in the channel and GDL is shown in Fig. 3.From this figure, it is clear that the pressure distribution in the channel decreases along the flow direction in the downstream. Pressure gradient through the GDL is observed when the pressure difference between adjacent two channels was large. Due to substantial pressure difference between two adjacent channels a large amount of flow crosses though the GDL under the rib is shown in Fig. 4Fig. 5(a) shows the total pressure drop from channel inlet to outlet for various pitch length with wide range of permeability. Here the porosity value is used fixed as 0.7. The effect of porosity with permeability $1.76d^{-11}m^2$ on the total pressure drop is depicted in Fig. 5(b). Fig. 5(a) shows the total pressure drop from channel inlet to outlet for various pitch length with wide range of permeability. Here the porosity value is used fixed as 0.7.

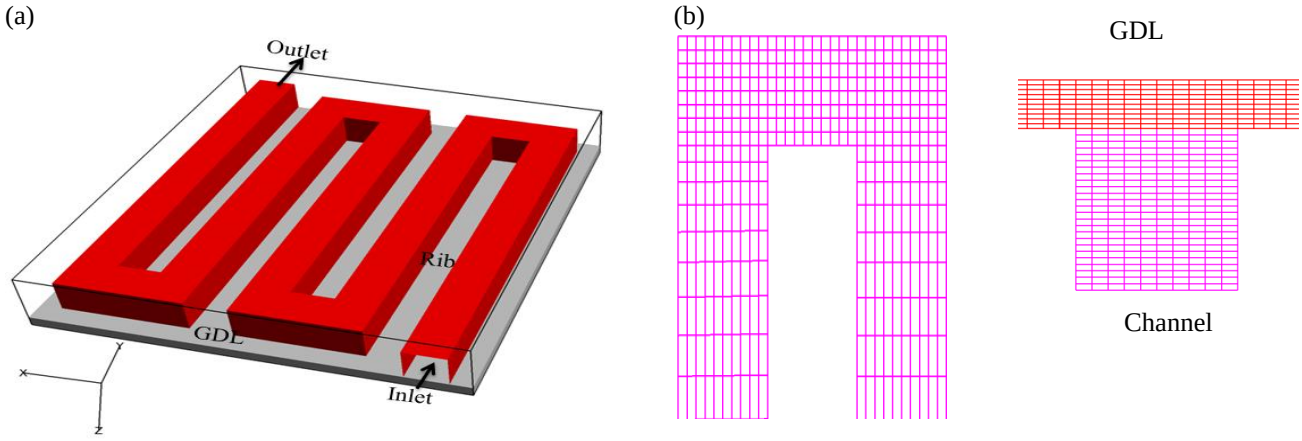

Fig. 1 (a) Computational domain with pitch length 1.0 mm and GDL (b) Grid arrangement of the numerical domain

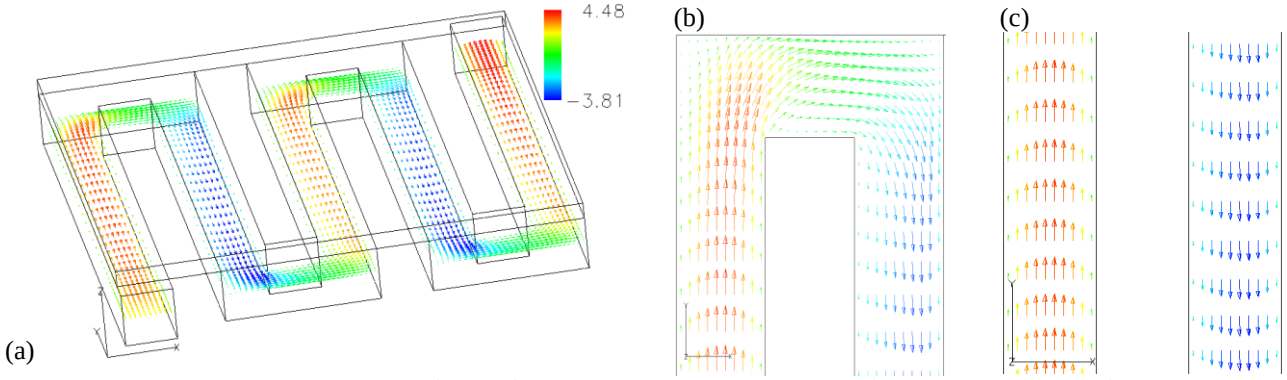

Fig. 2 (a)Velocity distribution at the mid-plane of the gas flow channel (b) Velocity at the corner of U-turn (c) at the middle of the channel

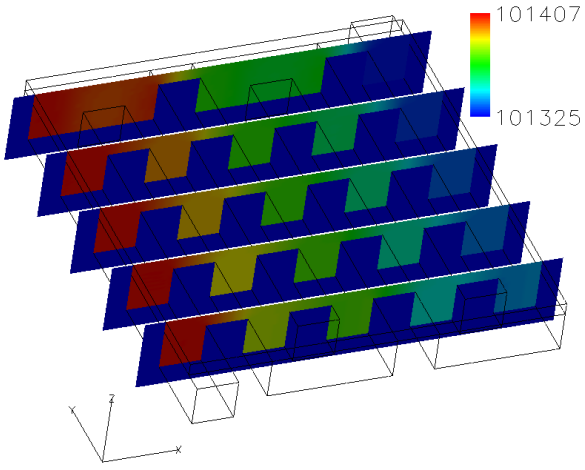

Fig. 3 Pressure distribution in the channel and GDL at several axial positions (y=2, 4, 6, 8, 9 mm from inlet)

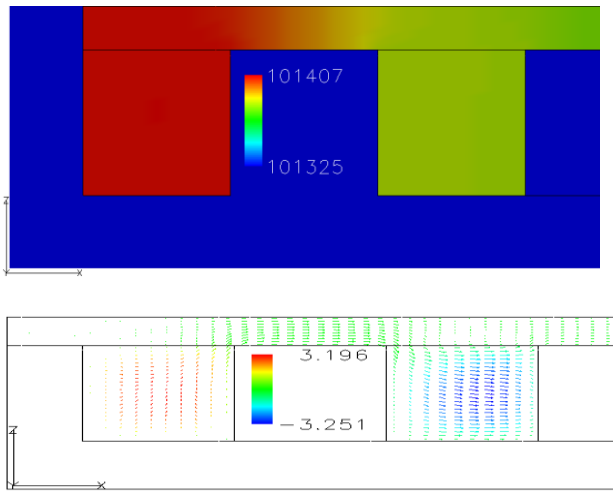

Fig. 4: Pressure distribution and velocity distribution in the channel and GDL on the x-z plane at y=2mm, with x=0 to x=4 mm

The effect of porosity with permeability $1.76d^{-11}m^2$ on the total pressure drop is depicted in Fig. 5(b). Three distinct pitch length of channel were considered in this simulation. The flow rate $Q = 2.0\times10^{-6}m^3$ /s remained constant in all cases. The flow rate is expressed as: Flow rate=Cross sectional area of channel inlet × Inlet velocity. The velocity becomes higher when we considered the inlet cross-sectional area is decreased by decreasing the pitch length. So, higher estimation of pressure derived from the higher estimation of velocity. Hence, the total pressure drop is increasing with decreasing of pitch length. On the other hand, for any values of pitch length the total pressure drop is decreasing with the increasing of permeability. This phenomenon can be explained by two ways: (1) Increasing the permeability, the ability of transmitting

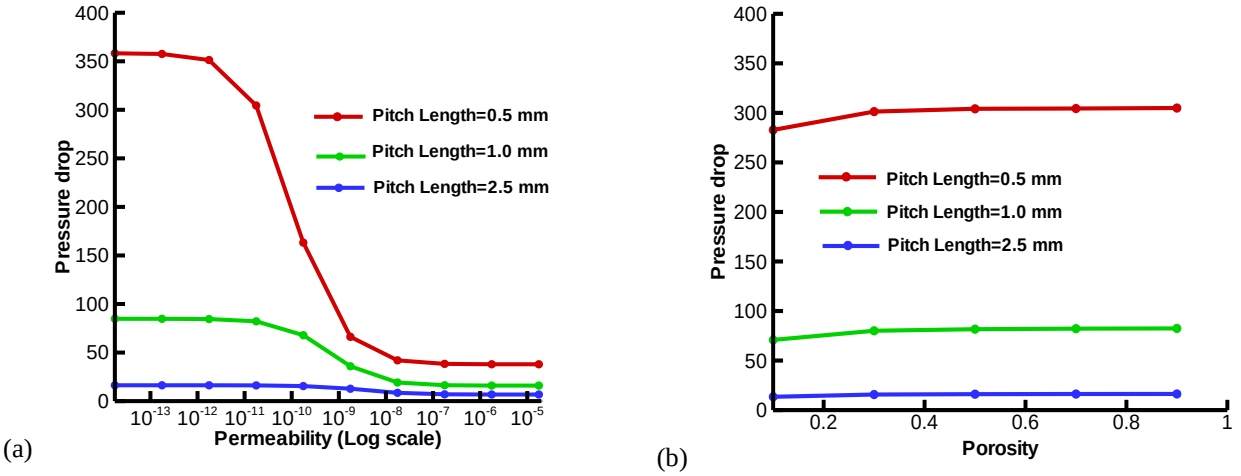

Fig. 5: The effect of pitch length on the pressure drop with (a) wide range of permeability (b) various values of porosity

This phenomenon can be explained by two ways: (1) Increasing the permeability, the ability of transmitting reactant gas to the gas diffusion layer is increased, and (2) The reactant gas transfer by flow cross-over through the GDL also increased. From fig. 5(b) it is evident that the total pressure drop variation very small for various values of porosity. The cross flow rate through the GDL under the rib is quantified as volume mass flux. The volume mass flux is calculated over the surface through the GDL under the rib near to outlet section. Fig. 6 (a) shows the ratio of cross flow rate to the total inlet flow rate for various thickness of GDL with varying permeability values and Fig. 6(b) for various pitch length. It can be seen that decreasing the thickness of GDL decreases the cross flow rate through the GDL while decreasing the pitch length increases the cross flow rate through the GDL. Fig. 7 shows the effect of GDL thickness on the total pressure drop with pitch length 1.0 mm. It is found that the highest pressure drop is obtained in the case of without GDL. The total pressure drop is decreased by the increasing of GDL thickness. It is thought that placing GDL on the channel, the reactant gas flows from channel to GDL by diffusion process. In order to explain the cross flow effect on pressure drop, it was considered the straight channel which length is the same as of serpentine channel with pitch length of 0.5 mm. From Fig. 8 it is clear that cross flow has a significant effect on pressure drop. Since straight channel has no cross flow, for this reason with increasing permeability values the pressure drop distribution from channel inlet to outlet is almost unchanged. However, in the serpentine channel the pressure drop is decreasing with increasing permeability values. For the very small values of permeability such as $1.76d^{-14}$ m^2 there is no cross flow in the serpentine channel. Obviously, there is no cross flow in the straight channel for any values of permeability. So, if we compare the red and orange curves in Fig. 8 we can confirm that the gap between two curves is the effect by bend region in a serpentine channel. Therefore, the bend region can improve the pressure drop in the serpentine channel.

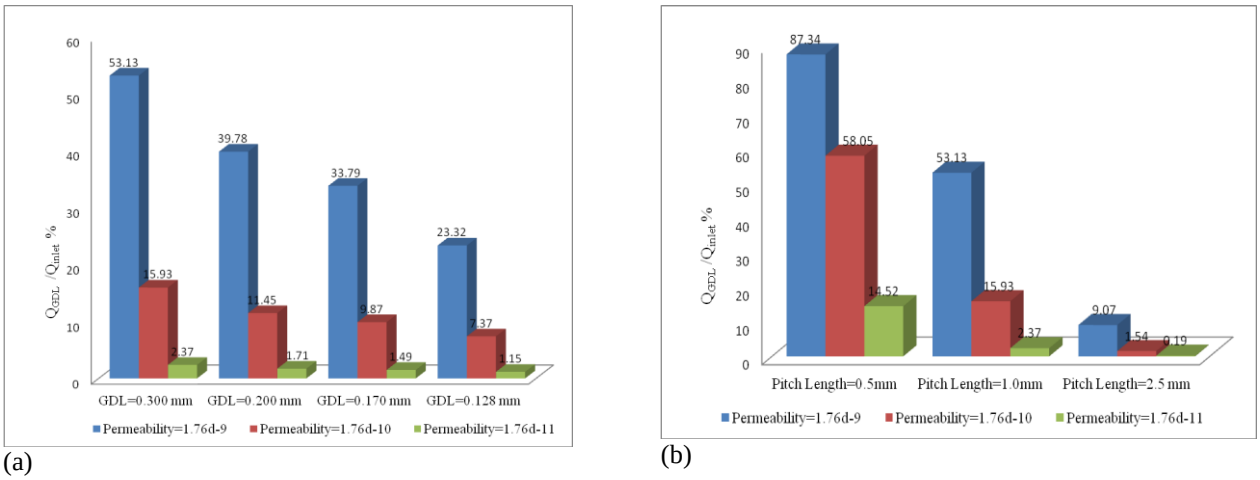

Fig. 6: Ratio of GDL cross flow rate to total intel flow rate (a) various GDL thickness with pitch length 1.0 mm (b) various pitch length with GDL thickness 0.3 mm

4. Conclusion: In this study, basic understanding of geometrical characteristics and physical properties of porous media

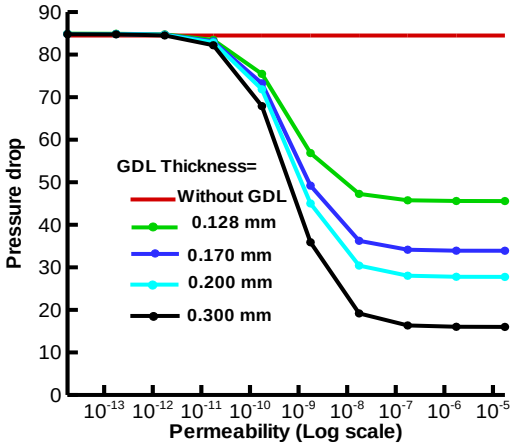

Fig 7: The effect of GDL thickness on total pressure drop from inlet to outlet with wide range of permeability values

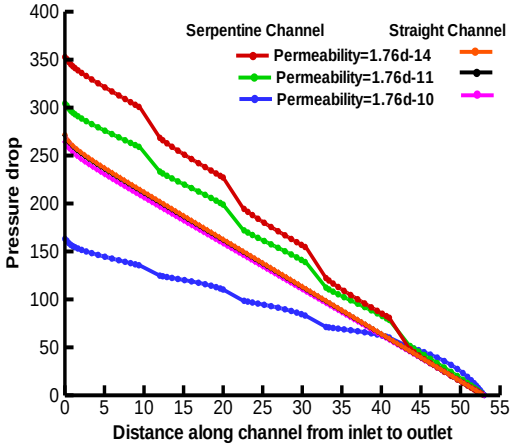

Fig. 8: The pressure drop distribution from channel inlet to outlet in the straight channel and in the serpentine channel

on the pressure loss mechanism and cross flow behavior has been clarified. We may summarize several conclusions as follows:

① The dependency of pitch length of serpentine channel is found significant on the pressure drop as well as cross flow.

② The pressure drop is increased with decreasing pitch length. The permeability has a strong effect on pressure drop. It is found that the pressure drop remain unchanged when permeability values smaller than 10^{-12} m^2 or larger than 10^{-8} m^2 Therefore, GDL behaves as porous media when the range of permeability values lies in between 10^{-12} and 10^{-8} m^2.

③ The effect of porosity on pressure drop and cross flow is indistinguishable.

④ Decreasing the thickness of GDL pressure drop increased while the amount of cross flow is decreased.

⑤ It is found that the bend region of serpentine channel can increase the pressure drop. On the other hand, cross-flow itself suppressed the pressure gradient. Therefore, increasing the number of bend region and using smaller pitch length of serpentine channel can improve the performance of polymer electrolyte membrane fuel cell.

⑥ The largest amount of cross flow is found for the pitch length of 0.5 mm, so the removal of produced water in a cell is higher for the pitch length 0.5 mm than other pitch lengths. On the other hand, the bend region play an important role for distributing pressure in the serpentine channel and bend region improve the pressure gradient.

References

[1] Kanezaki T., Li X., Baschuk J. J., "Cross leakage flow between adjacent channels in PEM fuel cells", *Journal of Power sources*, 2006, 162,415-425

[2] Shi Z., Wang X.,, "A numerical study of flow crossover between adjacent channels in a proton exchange membrane fuel cell with serpentine flow field", *Journal of Power Sources* ,2008,185, 985–992

[3] Sun L., Oosthuizen P. H., McAuley K. B., "A numerical study of channel-to-channel flow cross-over through the gas diffusion layer in a PEM-fuel cell flow system using a serpentine channel with a trapezoidal cross-sectional shape", *International Journal of Thermal Sciences* 2006, 45, 1021-1026

[4] Jiao K.., Park J., Li X., "Experimental investigations on liquid water removal from the gas diffusion layer by reactant flow in a PEM fuel cell", *Applied Energy* , 2010, 87, 2770-2777

[5] Bachman J., Santamaria A., Tang H., Park J., "Investigation of polymer electrolyte membrane fuel", *Journal of Power Sources*, 2012, 198, 143-148

[6] Saha L. K., Kurihara E., Oshima N., "Comparative studies of time-steeping schemes for the treatment of the Darcy drag term of the momentum equation", *Journal of Fluid Science and Technology*,2010,5 (2), 259-269

[7] Saha L. K., Tabe Y., Oshima N., "Effect of GDL deformation on the pressure drop of polymer electrolyte fuel cell separator channel", *Journal of Power Sources*, 2012, 202, 100-107

[8] Saha, L. K. and Oshima N."Prediction of flow crossover in the GDL of PEFC using serpentine flow channel", *Journal of Mechanical Science and Technology*,2012, 26(5), pp. 1315-1320

[9] Nishimura A., Shibuya K., Morimoto A., Tanaka S., Hirota M., Nakamura Y., Kojima M., Narita M., Hu E., "Dominant factor and mechanism of coupling phenomena in single cell of polymer electrolyte fuel cell", *Applied Energy*, 2012, 90, 73-79

[10] Mazumder S. and Cole J. V., "Rigorous 3-D Mathematical Modelling of PEM Fuel Cells", *Journal of the*

Electrochemical Society, 2003,150, A1503-1509

Available online at www.sciencedirect.com

SciVerse ScienceDirect

Procedia Engineering 00 (2012) 000–000

Procedia Engineering

www.elsevier.com/locate/procedia

5th BSME International Conference on Thermal Engineering

Heat Transfer Enhancement in an Air Process Heater using Semi-Circular Hollow Baffles

Aashique Alam Rezwan*, Sarzina Hossain, S M Ashrafur Rahman and MA Islam

Department of Mechanical Engineering, Bangladesh University of Engineering & Technology, Dhaka, Bangladesh

Abstract

Air process heater is one of the crucial equipment for many industries. Process heater is used in Baking, Drying, Laminating, Metal Working, Packaging, Plastic Welding, Preheating, Sealing, Soldering, Shrink Fitting, Synthetic Fabric Sewing and in other industries. But heating of air to a very high heat flux is sometimes impossible without the degradation of air quality, because many industries use combustion of gases for the purpose of heating the air to a very high heat flux. Electric heater can be alternative heating equipment, but it requires costly and long heating apparatus for the desired air temperature. In the present study, heat transfer enhancement in an air process heater was investigated both numerically and experimentally. A circular duct with 5 semi-circular hollow baffles and 4 cartridge electric heaters was designed for the process heating. Air was supplied from a wind tunnel at 3.17×10^4 Reynolds number. Total supplied electric power was 3 kW. The results showed the temperature ratio (Ambient Temperature/Air Temperature) to be decreased up to 0.72 where in many electric air heaters the temperature ratio is about 0.9. The designed air process heater supplies air at velocity 19 m/s and temperature up to 147ºC. The experimental results were also matched with the numerical simulation values of the designed heater. The results were also compared with some of the existing air process heater for investigating the enhancement of heat transfer.

Keywords: Air Process Heater; Heat Transfer Enhancement; Baffle; Cartridge Heater;

1. Introduction

Air process heater is important equipment in many industrial applications. Process heater is used in Baking, Drying, Laminating, Metal Working, Packaging, Plastic Welding, Preheating, Sealing, Soldering, Shrink Fitting, and Synthetic Fabric Sewing and in other industries. But heating of air to a very high heat flux is sometimes impossible without the degradation of air quality, because many industries use combustion of gases for the purpose of heating the air to a very high heat flux.

In the present study, a simulation approach has been conducted to increase the efficiency of the air process heater within size limit. The principle goal of the project is to design a heater that can be used to heat the air from a blower with certain velocity. The length of the heater is also a factor to be considered. The target length of the heater was given to be within 2 feet. Different types of combinations have been considered for the design, including using nicrome wire heater. But the calculated value showed that most of them can't be used due to inefficiency of heating to the air within the target range. Thus for better understanding and design, many complex geometry like series heater, heating by suddenly slowing down the air etc., has been simulated and compared. After several considerations finally the design with semi-circular hollow baffle showed a comprehensive improvement of the heating process within the target range.

* Corresponding author. Tel.: +8801552364999
E-mail address: aashiquear@gmail.com

Previously, similar type of heating system has been developed by MAT Ali and Hasan [1-2], but the capacity of the heating system is low compared to the present design [3]. Many other researchers has been experimented about the proper condition of an air process heater. Siviryuk et al. [4] has developed and diagnosis method for the air process heater, Vikhman et al. [5] has presented a technical and economic rationale for selecting an air process heater. The design process and the comparison of simulated value and the experimental value of the fabricated heater are described. The heater has been fabricated using the local available material and equipment, and the total fabrication has been done under the authors' supervision. The local availability of material and cost are also taken into consideration for the final design.

2. Design of Heater

Figure 1 shows the different parts of the heater section. The overall length of the heater section is 0.9 m. It consists of 4 cartridge heaters of total power consumption of 3 kW. Five half circular baffles are placed in series in the heating section to enhance the heating capacity of the air. Air from the wind tunnel is passed through the entrance section, heating section and settling chamber and then finally through the nozzle to produce the desired jet of air.

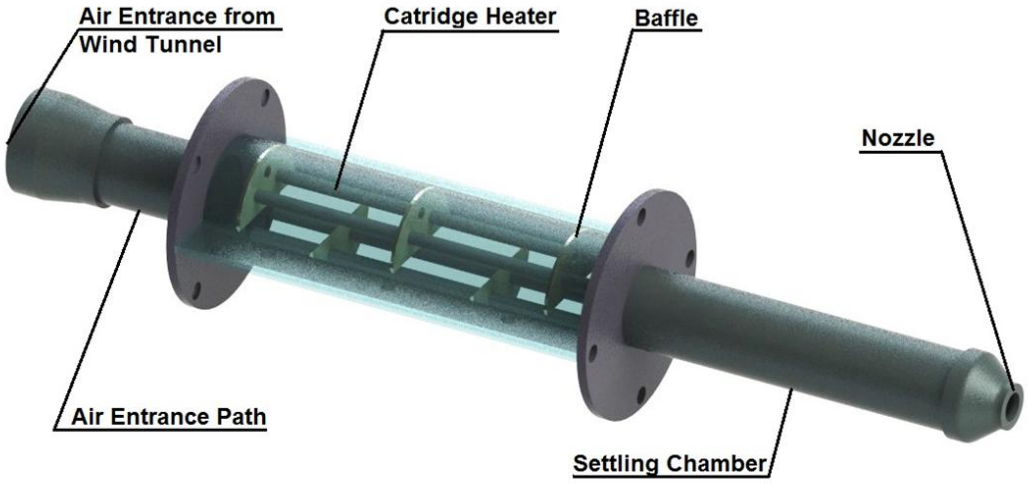

Fig. 1 Different Parts of the Heater Section

Swirling effect of the air due to the baffles ensures the uniform heating of air from the heater surface. The heated air then passes through the long settling chamber to the nozzle having a diameter of 25.4 mm. This is to note that the settling chamber is insulated with asbestos cloth and heat tape to prevent the heat loss to the surrounding from the hot air.

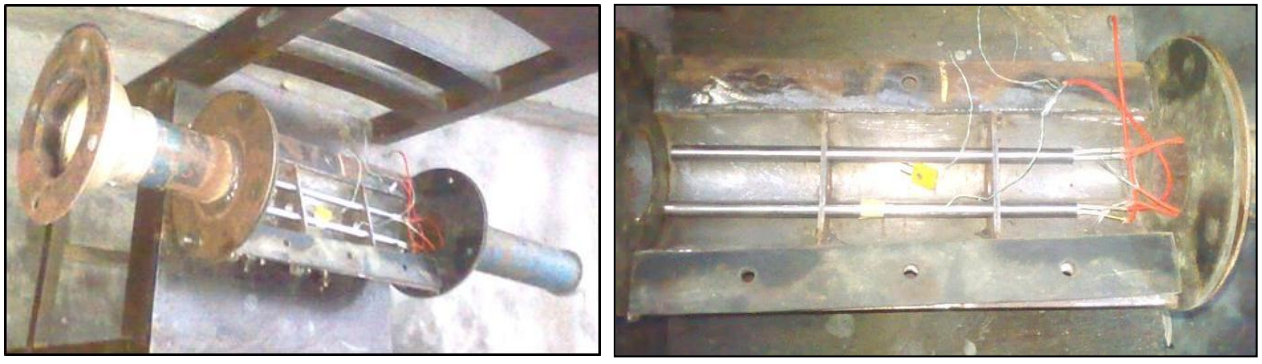

Fig. 2 Fabricated Heater Section [3]

3. Simulation of the Air Process Heater

For designing the heater computer simulation has been used. In the present works, ANSYS CFX has been used to simulate the air flow and heating process in the heater section. Figure 3(a) shows the contour plot of air temperature through the heater section. It can be seen that the swirling effect of the baffle greatly enhance the heating process.

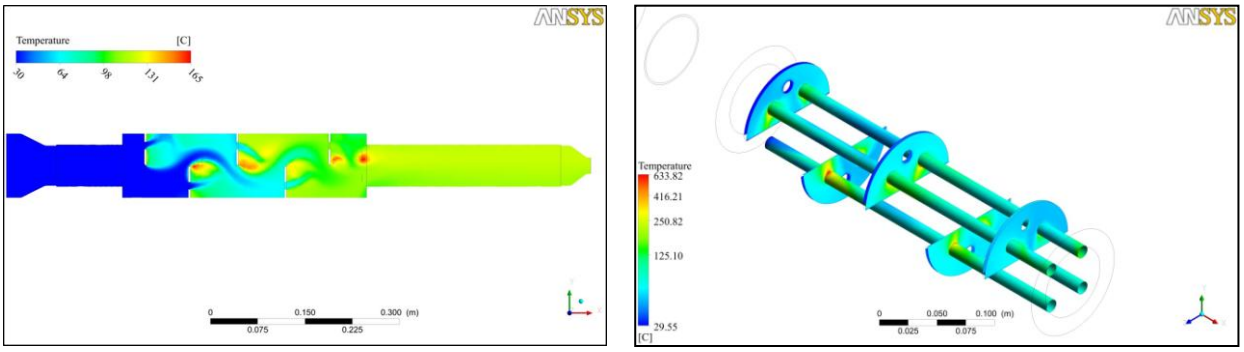

Fig. 3 (a) Temperature of Air through Heater Section (b) Heater Surface Temperature

In the fig. 3(b) the surface temperature of individual cartridge heater has been showed. This measurement is required for the safe heating of air. Due to the lack of heat transfer capability of air, the confined air in the section does not heat up properly. If the air near the surface of the heater can't transfer heat to the surrounding air in the section, the surface of the cartridge heater will be increase due to the lack of heat transfer. If the temperature increases in excess of the safe temperature for the heater, the heater could be break. Fig. 4 shows the mid line air temperature along the heater section.

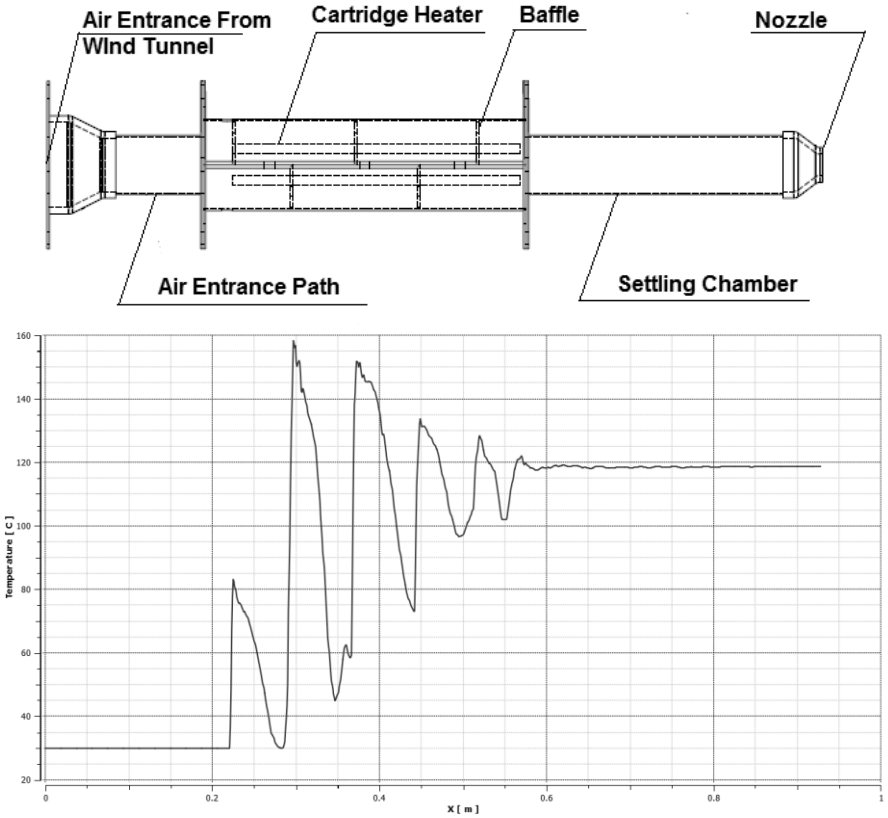

Fig. 4 Temperature of Air (mid line) along the Heater Section

4. Experimental Setup

The experimental study has been carried out by using a circular air jet facility as shown in Fig. 5. Detail explanation of different segment of the facility has been given in the previous studies [1-2]. The overall length of the flow facility is 9.0 m.

It has axial flow fan unit, two settling chambers, two diffusers, a silencer and a flow nozzle. The fan unit consists of three Woods Aerofoil fans of the same series. The fan unit receives air through the butterfly valve and discharges it into the silencer of the flow duct. Flow from the silencer passes on to the settling chamber through a diffuser. At the discharge, side of this chamber there is a flow straighter and wire screen of 12 meshes to straighten the flow and to breakdown large eddies present in the air stream. Air from this chamber then flows to the second settling chamber through a nozzle and second diffuser. The flow straighter and wire screens are used here to ensure a uniform axial flow free of large eddies which may be present in the upstream side of the flow. The flow from the second settling chamber then enters the 100 mm long and 80 mm diameter circular nozzle. At the farthest end the diameter of the flow facility is reduced from 475 mm to 88.9 mm where the heating section is placed [1-2].

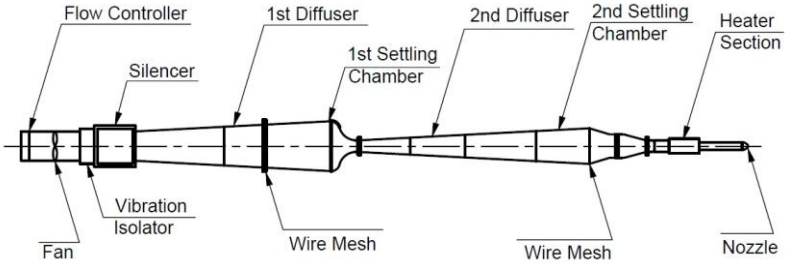

Fig. 5 Wind Tunnel for the Circular Jet Facility [1]

The air flow through the nozzle is controlled by regulating the speed of the fan units. The temperature of the jet is regulated by controlling the supply voltage of the heater. The whole setup is mounted on rigid frames of M.S. pipes and plates and these frames are securely fixed with the ground so that any possible unwanted vibration of the system is reduced to a minimum. To avoid the effect of ground shear, the setup is installed at an elevation of 1.4 m from the ground.

5. Results and Discussions

To ensure that the designed heater has been performing up to the requirement the heater section has been tested to its limit and compare with the computer simulation. Figures 6(a) depict the air jet temperature and fig. 6(b) temperature ratio of the jet of air for the increasing electrical energy input. With the increasing input energy the temperature of the jet of air increases exponentially. The surface temperature of the heater section (Fig. 6c) has been determined for the safety of the cartridge heater as described in the previous section. Then the experimental result has been compared with the computer simulation result. Fig. 7 shows the comparison between experimental result and the computer simulation result.

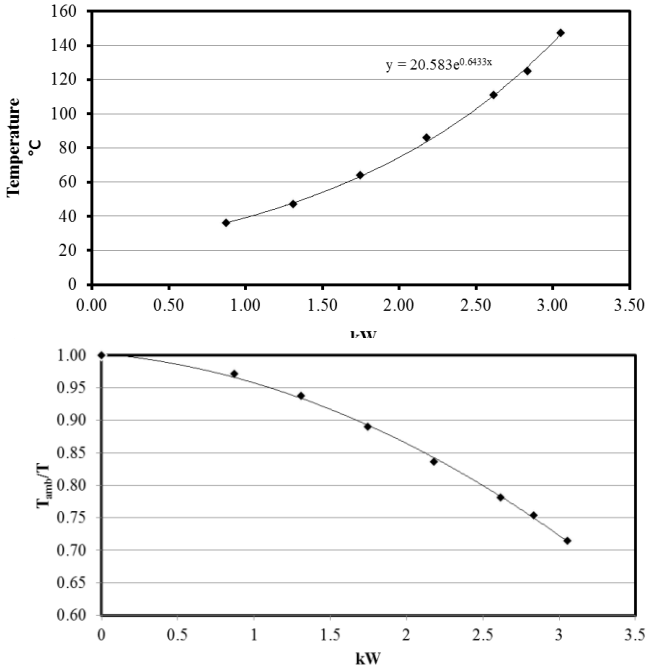

Fig. 6 (a) Temperature of Air Jet with Electrical Energy Input and (b) Temperature Ratio with Electrical Energy Input

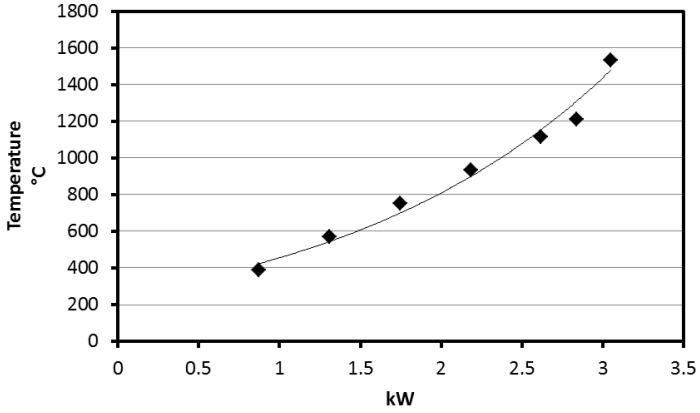

Fig. 6 (c) Temperature of Heater Surface with Electrical Energy Input

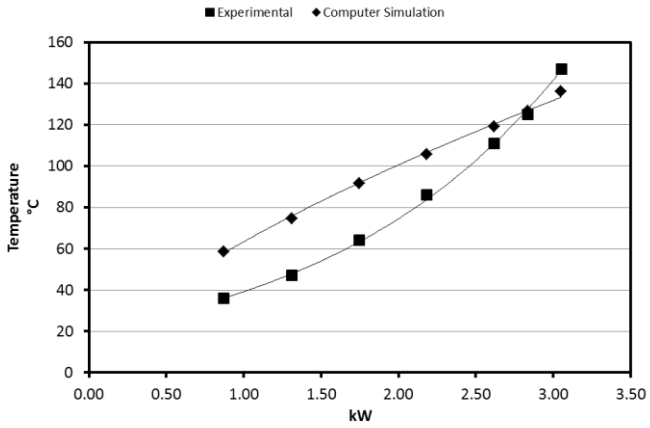

Fig. 7 Comparison between Simulation Result and Experimental Result

From the figure 7 it can be seen that at low power input, the temperature of air for the computer simulation is quite greater than the experimental result. As the power input increases, the difference between the two values also decreases and become equal at the rated condition for safe limit of the heater. After that, the experimental value of the temperature is increases more than the computer simulation result. This may due to the heat loss at low power, as there is cooler air in the surrounding. At high power input, as the time of heating increases, the temperature of the baffles and the pipe also increases. This restricts the air to loose heat to the surrounding environment.

Table 1. Summary of Previous & Designed Air Jet Heater Section [2]

Comparison Criteria	**Previous Heater [2]**	**Designed & Constructed Heater**	
		Simulation Value	**Experimental Value**
Heater Type	Electric Resistance Wire and Mica Sheet	Cartridge Heater 1200W (each)	
Number of Section	4	3	3
Number of Heaters	6	4	4
Maximum Design Capacity	3 kW	3 kW	3 kW
Maximum Capacity	-	4.8 kW	4.8 kW
$\frac{T_{amb}}{T}$ (minimum)	0.925	0.74	0.72
Maximum Jet Temperature	54°C	136°C	147°C
Re_d	3.72×10^4	3.17×10^4	3.17×10^4
Intermittent Mixing Capability	Present	Present	Present
Temperature Control	Varying the Supply Voltage	Given Input	Variable Voltage Supply

6. Conclusion

An air process heater has been designed and fabricated which can heat the air up to 147ºC. The designed Reynolds' number is 3.17×10^4.The surface temperature of the heater has also been determined for the safety limit of the heater. Total supplied electric power was 3 kW. The results showed the temperature ratio (Ambient Temperature/Air Temperature) to be decreased up to 0.72 where in many electric air heaters the temperature ratio is about 0.9. The designed air process heater supplies air at velocity 19 m/s and temperature up to 147ºC. The experimental results were also matched with the numerical simulation values of the designed heater. The results were also compared with some of the existing air process heater for investigating the enhancement of heat transfer. This type of heater can be adopted in any industrial process without adulterating the air.

References

1. Ali, M. A. T., Bhattacharjee, S., 2009, "Experimental Study of Thermally Stratified Co-Axial Jets with Trip Ring Excitation", *Proc. Int. Conf. on Mechanical Engineering (ICME2009), Dhaka, Bangladesh.*
2. Hasan, M. N., 2008, "Experimental Study of Flow Characteristics in the Near Field of a Thermally Stratified Co-axial Free Jet", M.Sc. Thesis, Bangladesh University of Engineering & Technology, Dhaka, Bangladesh.
3. Islam, MA, Rezwan, A.A., Hossain, S. and Islam, AKMN, 2011, "Study of Transient Heat Transfer of Solid with Protective Fabric Under Hot Air Jet Impingement", *Proc. Int. Conf. on Mechanical Engineering (ICME2011), Dhaka, Bangladesh.*
4. Siviryuk, V.L., Gramotnik, I.,V., and Bezrukov, A.,N., 2011, "Diagnostics of T\the Air-Heater Casings in Blast Furnaces.", Steel in Translation, Volume 41, Issue 1, pp36-40.
5. Vikhman, A.,G. and Kharichko, M.,A., 2006, "Selecting an Air Heater. Technical and Economic Rationale.", Chemistry and Technology of Fuels and Oils, Volume 42, Issue 4, pp 262-270.

Available online at www.sciencedirect.com

SciVerse ScienceDirect

Procedia Engineering 00 (2012) 000–000

Procedia Engineering

www.elsevier.com/locate/procedia

5th BSME International Conference on Thermal Engineering

In-cylinder Air Flow Characteristics Generated by Guide Vane Swirl and Tumble Device to Improve Air-Fuel Mixing in Diesel Engine using Biodiesel

Idris Saad*[a,b], S Bari[a], S N Hossain[a]

aBarbara Hardy Institute, School of Advanced Manufacturing and Mechanical Engineering, University of South Australia, Mawson Lakes Campus, South Australia, 5095, Australia
bFakulti Kejuruteraan Mekanikal, University Teknologi MARA, 40450, Shah Alam, Selangor, Malaysia

Abstract

In order to improve a naturally aspirated (NA) Compression Ignition (CI) engine operating on biodiesel fuel, this research proposes a Guide Vane Swirl and Tumble Device (GVSTD) inside the intake runner of a HINO W04D diesel engine to improve the in-cylinder air flow characteristic as an alternative solution to supplement existing techniques. When the air intake was guided in front of the intake port, organized turbulent air was generated, consequently assisting the fuel to evaporate and mix to produce better combustion and eventually produce better performance. To examine the effectiveness of the GVSTD, a 3D IC engine simulation model was developed. Additionally, this paper also investigates the optimal vane height of GVSTD of four vanes which twist at 35° clockwise direction and are arranged perpendicular to each other with the length of the vanes three times that of the intake radius. Ten simulation models of the GVSTD, where the vane height varied from 10% to 100% of the intake radius were prepared. The simulation results of in-cylinder pressure, turbulence kinetic energy and velocity of the base and all GVSTD models were then compared. The results illustrate a promising improvement of the in-cylinder air flow characteristics inside the fuel injected region by utilizing 20% vane height compared to standard model.

Keywords: Biodiesel; Engine Simulation; Guide Vane; Air-fuel mixing

Nomenclature

CI	compression ignition
GVSTD	guide vane swirl and tumble device
SOI	start of injection
TKE	turbulence kinetic energy
NA	naturally aspirated
TDC	top dead center
bTDC	before top dead center

1. Introduction

The properties of biodiesel fuel are found to be similar to the properties of conventional diesel fuel (Basha et al., 2009).

* Corresponding author. Tel.: +618 8302 5123; fax: +618 8302 3380.
E-mail address: saaiy003@mymail.unisa.edu.au

Therefore it can directly be used in a compression ignition (CI) engine with no or minor modifications (Idris Saad and Bari, 2011). Hence many researchers attempt to utilize this advantage. Among them, Celikten et al., (2010) compared CI engine performance fuelled with diesel, rapeseed and soybean fuels. The tests were conducted by using hydraulic dynamometer to the 4-cylinder direct injection CI engine. They found that, at standard injection pressure the engine fuelled by rapeseed and soybean experience a reduction of maximum power and torque of 1.0 kW and 2.1 N.m respectively compared to diesel. Additionally the fuel consumption of rapeseed and soybean were also reported to increase from diesel by about 29 g/kWh and 47 g/kWh, respectively. To improve these, they increased the fuel injection pressure up to 350 bar from the standard 250 bar. However, the performance of engine fuelled by rapeseed and soybean were still below the performance of engine fuelled by diesel even though they were improved from the previous tests. Although the CI engine was running on biodiesel, its performance was below the conventional diesel. This research is one of many examples (Bari et al., 2002a; Bari et al., 2004) which portray the colours of CI engine running with biodiesel fuel. Hence a conclusion can be made that none of the researchers provide the solution to solve many problems associated with CI engine running with biodiesel fuel.

These problems are mainly due to the inferior chemical properties of biodiesel compared to the conventional diesel fuel. The viscosity and density of biodiesel were reported to be higher and volatility lower than diesel fuel (Agarwal, 2007; Candeia et al., 2009; Idris Saad and Bari, 2011; Jaichandar and Annamalai; Rizalman Mamat et al., 2009) which lead to the incomplete combustion and this eventually produces lower engine performance and affects the durability of the engine (Bari, 2004; Bari et al., 2002b). This is one of the reasons why a CI engine running with biodiesel fuel suffers from such negative viewpoints. The researches in this area are focused to improve the properties of biodiesel by using additives (Moser, 2008), pre-heating the fuel to level its viscosity to that of diesel (Pugazhvadivu and Jeyachandran, 2005) and adjusting the injection timing (Ye and Boehman, 2012). Instead of duplicating what has been done, this paper investigates the capability of Guide Vane Swirl and Tumble Device (GVSTD) to improve the in-cylinder air characteristics to eventually improve evaporation, mixing and combustion process to improve the engine performance.

Previous study (Idris Saad and Bari, 2011) shows that the GVSTD possess high potential to improve the in-cylinder air characteristics when the results from the simulations were analysed. The GVSTD design of simulation model is comprised of four main parameters; vane height, vane angle, vane number and vane length. To capitalize on the previous study, this paper presents additional detailed study about the effect of vane height to generate better in-cylinder air characteristics. Ten GVSTD models were developed with its vane heights varying equally by 10% to 100% from radius of intake runner. Hence, it will provide better analyses and discussions in terms of optimization of the vane height.

Simulation results of the in-cylinder pressure, Turbulent Kinetic Energy (TKE) and velocity before the start of injection (SOI) until the part of expansion process were presented, compared and discussed before the optimum vane height to the 35° twist angle, four vane arrange perpendicular to each other with length three time that of the radius of intake runner was decided. The main contribution of this paper is that a lower vane height will provide better in-cylinder air flow characteristics rather than higher vane height which give more resistance to the flow instead of generating more swirl and tumble.

2. Methodology

A computer simulation of 3D cold flow fluid dynamic was used in this research to study the in-cylinder air flow characteristics generated by GVSTD. The proses of simulation included developing simulation models, performing the meshing to the model before setting up the boundary condition and running the simulation. The model was a duplicate from the naturally aspirated (NA) CI generator engine made by HINO with model of W04D running constantly at 1500 rpm. The engine data and simulation model is given in Table 1a.

Table 1. (a) Technical specification of engine model – HINO W04D; (b) Specification of GVSTD models.

(a)		(b)	
Engine Parameters	Value	GVSTD Parameters	Value
Bore × Stroke	104 × 108 mm	Number of Vanes (N)	4 vanes 90° to each other
Compression Ratio	17.9	Vane Twist Angle (θ)	35° Clockwise
Intake System	Naturally Aspirated	Intake Runner Radius (R)	10 mm
Piston Head	Bowl with Cone	Length of Vane (l)	3R
Start of Injection	14°bTDC	Height of Vanes (H)	0.10R, 0.20R, 0.30R, 0.40R, 0.50R 0.60R, 0.70R, 0.80R, 0.90R, 1.00R

As for preparing the simulation model, SolidWorks 2010 was utilised to draw the six components of the model; intake runner; intake port; intake valve; cylinder; exhaust valve and exhaust port. These components were then assembled together before being transferred into the ANSYS-DesignModeller 14 to assign its material to their domains. Both valves were assigned as solid parts such as the real component while others components were the fluids domains from the actual parts. That model is identified as the base model and denoted as 0.00R and illustrated in Fig.1a. The GVSTD models were then developed based on the specifications given in Table 1b and imposed in front of the intake port as shown in Fig.1b.

The cylinder of the engine simulation needed to run as moving mesh to replicate the motion of a piston as in a real engine, hence the model required a very fine mesh to perform this action. Therefore, the meshing for the entire model was included as a "refinement option" to ensure that all the tetrahedron elements are adequate especially on the surface of the cylinder wall.

The transient simulation was tested up to two cycles by using ANSYS-CFX 14. The continuity, momentum and energy equations used to compute this simulation and can be found in the ANSYS Solver Theory Guide (ANSYS INC, 2009). The initial condition of velocity, pressure and temperature were 0 m/s, 1 atm and 300 K respectively. In order to satisfy the discrete equations, the convergence criteria were set at 1×10^{-4} and the maximum coefficient loop was 500. However, the computation for each time step converged at approximately 15 coefficient loops.

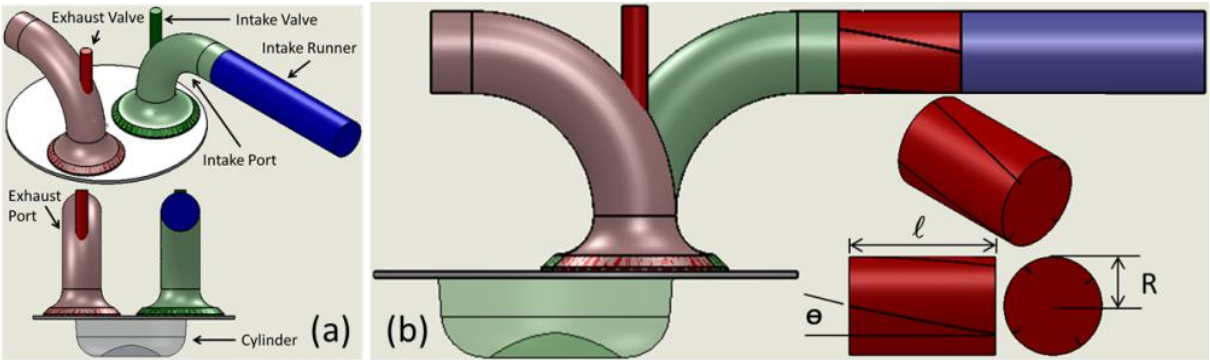

Fig.1. (a) Simulation model (0.00R); (b) Sample design of GVSTD and it assembly to the model.

3. Results and Discussions

In order to study the characteristics of the in-cylinder air flow, the results of in-cylinder pressure, TKE and the velocity were presented. These parameters were observed from 5°CA before SOI until 5°CA after top dead center (TDC). Based on Table 1a, SOI was set at 14°CA bTDC, hence the range of data will cover from 341°CA to 365°CA. This condition is vital since the main objective of imposing GVSTD is to generate better in-cylinder air flow characteristics to stimulate the atomization, evaporation and mixing processes by mean reducing the penetration and expanding the cone angle of injected fuel core and breaking-up the molecular chain of the fuel atoms (Heywood, 1988). Therefore those data were presented and discussed below.

3.1. In-cylinder pressure

The in-cylinder pressure will play an important role to improve the combustion efficiency. Higher in-cylinder pressure will reduce the fuel penetration during injection and expand the cone angle which is needed for higher viscous biodiesel. To analyze the in-cylinder pressure developed by GVSTD compared to the 0.00R, the curve of maximum pressure for all models is presented in Fig 2. Figure shows that the variation of in-cylinder pressure is not in order with the variation of vane height. This pattern of inconsistency was also found by Miles (2000) when swirl ratio were varied to 1.5, 2.5 and 3.5 on high-speed direct injection diesel engine by throttling low, medium and high helical intake port, respectively. Their result of in-cylinder pressure from Ricardo optical research engine was dominated by low throttling, followed by high throttling and medium throttling (Miles, 2000). Similarly, this research also found that GVSTD 0.20R which only have 2 mm of vane height produces the highest in-cylinder pressure. Furthermore, this 0.20R is the only model to generate in-cylinder pressure higher than 0.00R. With this result, higher in-cylinder pressure will definitely give more resistance to the injected fuel and

reduce the penetration length as well as expanding the cone angle as required by biodiesel fuel (Heywood, 1988) to improve the combustion.

The other models did not produce higher in-cylinder pressure than 0.00R; because higher vane heights gave more resistance in terms of friction to the air flow. This resistance reduced the ability of the air to enter the cylinder, consequently reducing its volumetric efficiency and also reducing the generated pressure with the same compression. However, the maximum reduction of highest in-cylinder pressure of about 2.8 % from 0.00R occurred with GVSTD 0.70R. According to Heywood (1988) CI engine normally runs with excess air, therefore with 2.8 % maximum reduction which considerably low as the pressure is almost 50 bar, it is believed that all the GVSTD models can still provide enough air to ensure sufficient combustion.

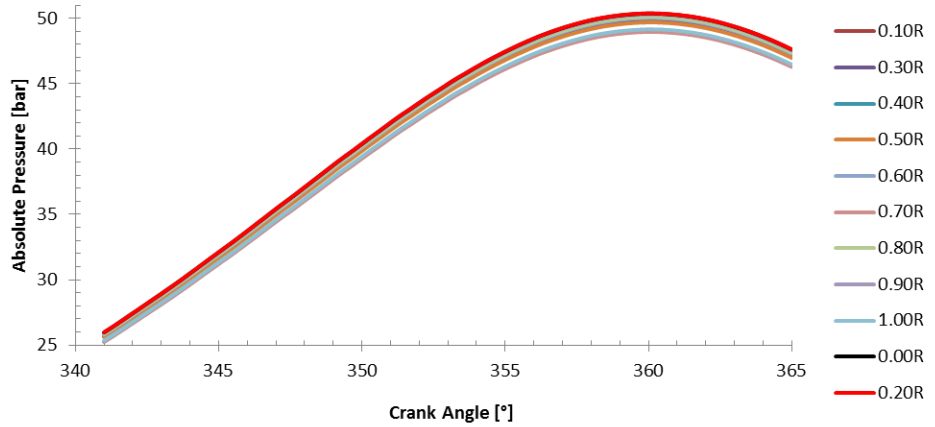

Fig.2. Curve of maximum in-cylinder pressure from 341°CA to 365°CA for various models.

3.2. In-cylinder TKE

TKE is the mean kinetic energy associated with eddies in turbulent flow per unit mass (White, 2011). Hence, higher in-cylinder TKE will provide more energy of eddies which can be used in the breaking-up of chains of fuel molecules. Figure 3 presents the curves of maximum TKE for all models as compared to 0.00R.

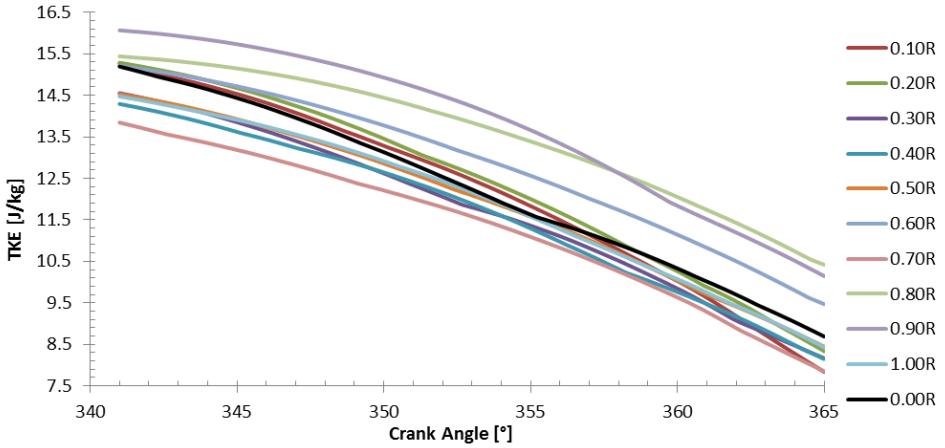

Fig.3. Curve of maximum in-cylinder TKE from 341°CA to 365°CA for various models.

Based on Fig 3, the maximum in-cylinder TKE almost linearly declines in this range of study toward the end. Research made by Payri et al., (2004) also shows similar pattern as they investigate the in-cylinder flow for direct injection diesel engine by using simulation with PISO algorithm. To justify their finding, laser Doppler Velocimetry was used to capture the image in the experiment. They found that both results were in an appropriate agreement (Payri et al., 2004). Not only that, Prasad et al., (2011) also presented similar shape of the in-cylinder TKE. Their research compared the swirl generated from

various shapes of piston bowls. AVL Fire software was used to determine the in-cylinder air flow characteristic (Prasad et al., 2011). Therefore, the finding in this research does not conflict with other researchers as the pattern of TKE is similar with both the simulations and experiments performed by others.

In terms of generating higher TKE, GVSTD 0.90R dominate the result until 356°CA before GVSTD 0.80R take over after that. Generally, five GVSTD models including GVSTD 0.20R provide better TKE before TDC, however only three of them can sustain until 365°CA. Unlike the in-cylinder pressure, a higher vane height will produce better TKE as the results show for GVSTD 0.60R, 0.80R and 0.90R. It does not mean that the lower vane height cannot produce higher TKE than without GVSTD, but it is not high enough to sustain a TKE better than 0.00R until the expansion process as witnesses by GVSTD 0.10R and 0.20R in Fig 3. Therefore, GVSTD is successful to generate better TKE than the standard model.

3.3. In-cylinder velocity

After the injected fuel reduces its penetration length and expands its cone angle by higher in-cylinder pressure and breaks up the molecule chains by higher TKE, it is time to investigate the velocity of in-cylinder air to induce the mixing process. As such, Fig 4 illustrates the behavior of in-cylinder velocity for all models.

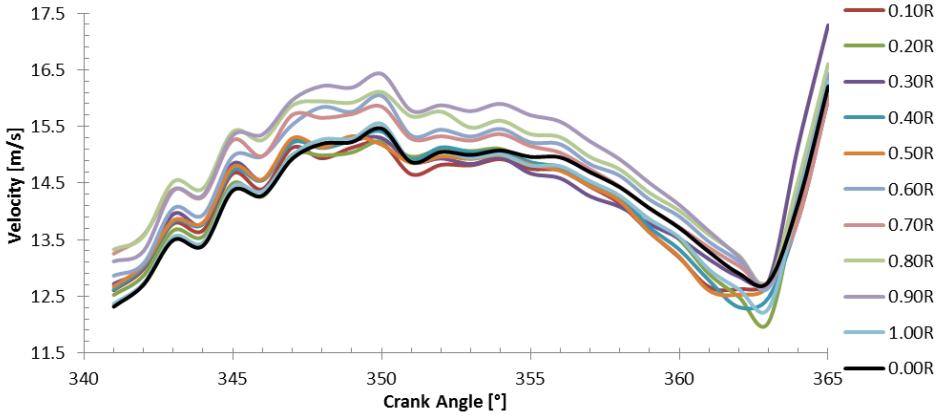

Fig. 4. Curve of maximum in-cylinder velocity from 341°CA to 365°CA for various models.

As illustrated in Fig 4, all GVSTD models provide higher in-cylinder velocity than 0.00R until 347°CA. However the results of GVSTD 0.60R and 0.80R have better results than 0.00R for the whole range of analysis. The dome shape of velocity curve occurs before TDC because when the piston is compressing the air, it will enhance the velocity but when piston keeps moving, it reduces the available cylinder volume for the air to move. After that, piston is moving toward BDC and it increases the cylinder volume thus allowing the fluid to move again. The significant results of increasing the in-cylinder velocity by GVSTD in this study will definitely help the mixing processes and improve the performance of NA CI engine operating on biodiesel fuel.

3.3. Selection of GVSTD model

GVSTD 0.90R generated the best result of TKE and better velocity than GVSTD 0.00R until TDC but its in-cylinder pressure is below GVSTD 0.00R. As for GVSTD 0.60R and 0.80R, their results for TKE and velocity are above GVSTD 0.00R. However, their results for pressure are not greater than GVSTD 0.00R. The only model which improves all in-cylinder parameters is the GVSTD 0.20R. With a relatively small vane, the GVSTD 0.20R is capable of increasing the in-cylinder pressure, TKE and velocity. Therefore, this study admits that the best GVSTD to provide better in-cylinder air flow characteristics so far is the GVSTD 0.20R. These improvements conform to the requirement of improving the mixing process of NA CI engine which is needed to improve the engine performance (Heywood, 1988). Therefore, the modification to the NA CI engine by using GVSTD 0.20R will help solving or reducing the problems mentioned above when fuelled by biodiesel fuel especially when combined with existing techniques.

4. Conclusions

Based on the weaknesses from the results from the current techniques used to improve the air-fuel mixing process in NA CI engine running on biodiesel fuel by researchers worldwide, this paper presented the technique to improve it is by using

GVSTD. To prove the capability of this technique, ten GVSTD simulation models with various vane heights were developed and their results were compared with the simulation model without GVSTD. After the results of in-cylinder pressure, TKE and velocity were presented and discussed, this study found that the best GVSTD model is the one having 20% of vane height to the intake radius, 35° twist angle, four vane 90° to each other and three times length of the intake radius. With this configuration, all three in-cylinder parameters discussed above were improved. Therefore, this research believes by using GVSTD 0.20R, the performance of NA CI engine using biodiesel as a fuel can be increased especially when combined with other techniques performed by other researchers.

Acknowledgements

The first author acknowledged the Universiti Teknologi MARA and Ministry of Higher Education, Malaysia for the scholarship granted to undertake this research.

References

[1] Agarwal, A.K., (2007). Biofuels (alcohols and biodiesel) applications as fuels for internal combustion engines. Progress in Energy and Combustion Science 33(3), 233-271.
[2] ANSYS INC, (2009). CFX-Solver Theory Guide, in: 12.1, R. (Ed.).
[3] Bari, S., (2004). Investigation into the deteriorated performance of diesel engine after prolonged use of vegetable oil, *ASME 2004 Internal Combustion Engine Division Fall Technical Conference* ASME, Long Beach, California, USA.
[4] Bari, S., Lim, T.H., Yu, C.W., (2002a). Effects of preheating of crude palm oil (CPO) on injection system, performance and emission of a diesel engine. Renewable Energy 27(3), 339-351.
[5] Bari, S., Yu, C., Lim, T., (2002b). Filter clogging and power loss issues while running a diesel engine with waste cooking oil. Proceedings of the Institution of Mechanical Engineers, Part D: Journal of Automobile Engineering 216(12), 993-1001.
[6] Bari, S., Yu, C., Lim, T., (2004). Effect of fuel injection timing with waste cooking oil as a fuel in a direct injection diesel engine. Proceedings of the Institution of Mechanical Engineers, Part D: Journal of Automobile Engineering 218(1), 93-104.
[7] Basha, S.A., Gopal, K.R., Jebaraj, S., (2009). A review on biodiesel production, combustion, emissions and performance. Renewable and Sustainable Energy Reviews 13(6-7), 1628-1634.
[8] Candeia, R.A., Silva, M.C.D., Carvalho Filho, J.R., Brasilino, M.G.A., Bicudo, T.C., Santos, I.M.G., Souza, A.G., (2009). Influence of soybean biodiesel content on basic properties of biodiesel–diesel blends. Fuel 88(4), 738-743.
[9] Heywood, J.B., (1988). *Internal Combustion Engines Fundamentals*. McGraw Hill International.
[10] Idris Saad, Bari, S., (2011). Effects of Guide Vane Swirl and Tumble Device (GVSTD) to the Air Flow of Naturally Aspirated CI Engine, in: Prof. Mohammad Ali (Ed.), *International Conference on Mechanical Engineering 2011 (ICME2011)*. Progressive Printers Pvt. Ltd., Dhaka, Bangladesh.
[11] Jaichandar, S., Annamalai, K., Effects of open combustion chamber geometries on the performance of pongamia biodiesel in a DI diesel engine. Fuel(0).
[12] Miles, P.C., (2000). The influence of swirl on HSDI diesel combustion at moderate speed and load. SAE International Journal.
[13] Moser, B.R., (2008). Influence of Blending Canola, Palm, Soybean, and Sunflower Oil Methyl Esters on Fuel Properties of Biodiesel†. Energy & Fuels 22(6), 4301-4306.
[14] Payri, F., Benajes, J., Margot, X., Gil, A., (2004). CFD modeling of the in-cylinder flow in direct-injection Diesel engines. Computers & Fluids 33(8), 995-1021.
[15] Prasad, B.V.V.S.U., Sharma, C.S., Anand, T.N.C., Ravikrishna, R.V., (2011). High swirl-inducing piston bowls in small diesel engines for emission reduction. Applied Energy 88(7), 2355-2367.
[16] Pugazhvadivu, M., Jeyachandran, K., (2005). Investigations on the performance and exhaust emissions of a diesel engine using preheated waste frying oil as fuel. Renewable Energy 30(14), 2189-2202.
[17] Rizalman Mamat, Nik Rosli Abdullah, Hongming Xu, Miroslaw L. Wyszynski, Athanasios Tsolakis, (2009). Effect of Air Intake Pressure Drop on Performance and Emissions of a Diesel Engine Operating with Biodiesel and Ultra Low Sulphur Diesel (ULSD), *International Conference on Renewable Energy and Power Quality (ICREPQ'09)*, Valencia, Spain.
[18] White, F.M., (2011). *Fluid mechanics* (7th ed. ed). McGraw Hill, New York, N.Y.
[19] Ye, P., Boehman, A.L., (2012). An investigation of the impact of injection strategy and biodiesel on engine NOx and particulate matter emissions with a common-rail turbocharged DI diesel engine. Fuel 97(0), 476-488.

Available online at www.sciencedirect.com

SciVerse ScienceDirect

Procedia Engineering 00 (2012) 000–000

Procedia Engineering

www.elsevier.com/locate/procedia

5th BSME International Conference on Thermal Engineering

Experimental study of interaction between supersonic duct flow and jets and rods surrounded by the porous cavity

Nao Kuniyoshi[a], Minoru Yaga[b]*, Isao Teruya[b], Msaaki Ishikawa[b]

[a]*Graduate Schools of Engineering of Science University of the Ryukyus, 1 Senbaru, Nishihara Okinawa 903-0123, Japan*
[b]*Department of Mechanical system Engineering University of the Ryukyus, 1 Senbaru, Nishihara Okinawa 903-0123, Japan*

Abstract

In this study, an experiment was performed to clarify the flow field, in which the jets or rods were normally injected into a main supersonic flow surrounded by a porous cavity, and this report figures out flow direction and stability in the cavity with thermal tuft probe. In the experiment, a porous cavity is attached to a main duct and rods or jets are inserted to the main duct on the porous cavity. To reveal this flow field, the thermal tuft probe was adopted to experimentally investigate the flow direction in the cavity. In addition to the experiment with the jets, the experiments with rods instead of jet were conducted. In the experiments, the effect of the combination of jets or rods and a porous cavity is studied by means of visualization of schlieren method, pressure distributions and the flow direction in the cavity with the thermal tuft probe. Three cases for arrangements are tested in the experiments. As the results, it is found that the flow direction in the cavity is greatly influenced by the starting shock wave position and the rod or jet. The pressure ratio at which the starting shock wave passes through the porous cavity is affected by the jets and rods. Moreover it is found that the flow in the cavity is influenced by the jet and rod even after the starting shock wave move downstream of the porous cavity.

Keywords: Shock wave, Compressible flow, Porous cavity, Jet, Rod

Nomenclature

h	height (mm)
x	distance from throat (mm)
p	pressure (Pa)
d	diameter of hole (mm)
Subscripts	
0	stagnation condition
b	ambient condition
L	shock wave condition
S	shock wave condition
c	cavity condition
p	thermal tuft probe condition
Superscript	
*	throat condition

* Corresponding author. Tel.: +81-98-895-8617; fax: +81-98-895-8707.
E-mail address: yaga@tec.u-ryukyu.ac.jp

1. Introduction

Supersonic mixing enhancements have attracted a great deal of attention because of the potential for important applications to scram jet engines [1] and thermal sprays [2], for example. A number of studies have investigated the mixing process under the supersonic state using various techniques, such as the use of a swept ramp [3], and a use of a wedge shaped injector [4]. However, a number of problems, such as mixing losses, mixing efficiency [5], remain. The authors previously proposed a new concept, as shown in Fig. 1, whereby the losses of the flow field in the mixing process might be reduced [6, 7]. In the first stage, the jet is injected in a direction normal to the main flow. The jet is considered as an obstacle to the main supersonic flow. Then a bow shock wave is generated and causes a pressure difference between the upstream and downstream sides of the shock wave. Pressure differences also exist on the porous wall and inside the cavity, which drives the flow in the cavity. At the same time, together with the main flow, the injected jet is sucked into the cavity through the porous holes. The flow velocity in the cavity is reduced enough to allow mixing of the injected jet and the main flow. The flow in the cavity is spouted again, achieving small fine injections through numerous small porous holes. In order to figure out the effect of the jets on the flow field experimentally in the cavity, the relatively high frequency device for measuring the flow direction, so called thermal tuft probe was adopted. This device is based on the concept of directional sensitive hot-wire probe reported by C. P. Häggmark [8]. The difference between the thermal tuft probe and a directional sensitive hot-wire probe is the function of measuring the flow velocity itself. That is, the device can detect the only flow direction. To reveal the flow field, it is necessary to investigate the flow direction in the cavity. The probe is a high response sensor and can detect one dimensional flow direction. Therefore, we herein focus mainly on the flow direction in the cavity. In addition to jets, experiments with rods instead of jets were performed.

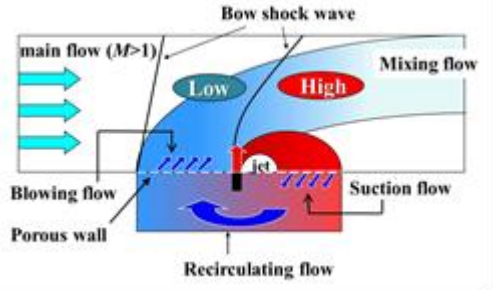

Fig. 1. Schematic diagram of a previously proposed loss reduction concept

2. Experimental apparatus and procedure

2.1. Wind tunnel facility

Figure 2 shows a schematic diagram of the experimental apparatus used in the present study. The blow-down wind tunnel was used for this experiment. The schlieren method was performed using a xenon spark light source to visualize the density field. Twenty pressure taps were positioned on the upper wall, along the center of the duct. The taps were scanned with a pressure scanning device. Schematic diagrams of the nozzle and the test section are shown in Fig. 3. The test section is attached to a diverging nozzle with a designated Mach number of 2.2. The test section has a diverging angle of 1° for each side in order to avoid large amplitude oscillations of a starting shock wave. The x direction, along the flow direction originating at the throat, is non-dimensionalized by the nozzle throat height h^*. A cavity with a porous wall is installed within the range of $x/h^* = 7.0$ to 11.4. The depth of the cavity is $h_c/h^* = 1$. The diameter d and the pitch of the holes of the porous wall are 1 mm and 2 mm, respectively. Eleven holes are distributed in the streamwise direction and fifteen holes are distributed in the spanwise direction. The porosity, which is defined as the ratio of the total area of the holes to the porous region, is approximately 0.617. Jets and rods are inserted from the porous region. Figures 4(a) through 4(c) show the arrangements of the jets and rods. The jets and rods are positioned at $x/h^* = 8$ and 9.2 and the diameters of the jets and rods are 1 mm.

2.2. Thermal tuft probe

In this experiment, the relatively high response and small device for the measurements, so called thermal tuft probe is adopted. Images of the thermal tuft probe are shown in Fig. 5. The heating wire and the two sensors for the heat detection are made of Moleculoy(φ1 mm) and tungsten(φ0.005 mm), respectively. The distance between the heating wire and each sensor is 0.5 mm. An electronic circuit of the thermal tuft probe is shown in Fig. 6. The sensors are connected with

Wheatstone bridge. The resistances of the sensors change with heat conveyed from the heating wire to the sensors by the flow, which generates bridge voltage change. This voltage change contains information about the flow direction. The heat detectors and the heating wire cannot be used to measure the absolute flow velocity due to a lack of their calibrations. In this experiment, the heat detectors can only detect a streamwise flow direction in the cavity. And it was proved that the thermal tuft probe used in the experiment does not disturb the flow[9].

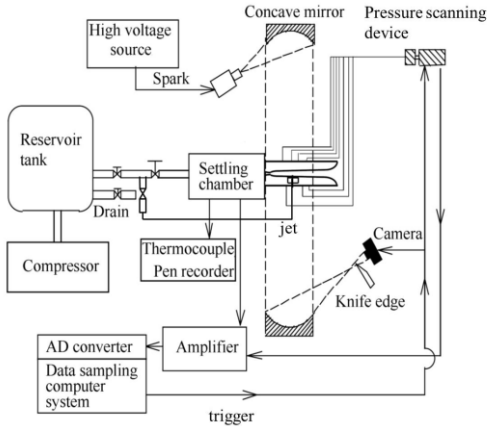

Fig. 2. Experimental apparatus

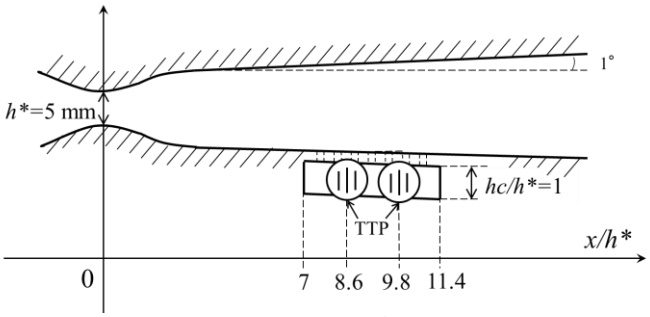

Fig. 3. Schematic diagram of test section

2.3. Experimental and measurement condition

The experiments were conducted for wind tunnel pressure ratios p_0/p_b of between 2.0 and 3.0, where the pressure ratio p_0/p_b is defined as the ratio of the stagnation pressure p_0 in the settling chamber to the back pressure p_b. In the experiments, flow direction measurements with the thermal tuft probe and static pressure on the upper wall were conducted for p_0/p_b of 2.0 through 3.0 and at p_0/p_b=3.0, respectively. The thermal tuft probe is installed at x/h^* = 8.6 and 9.8 in the cavity as shown in Fig. 3. The sampling number and interval of the output from the thermal tuft probe are 4096 and 100 μs at each pressure ratio, respectively. In the static pressure measurement, the average of the pressure is taken for three patterns 000, Jet111 and Rod111. At the same time, the density field was visualized by the schlieren method. The jet-to-freestream momentum flux ratio for each jet was $J \approx 1.9$ where the freestream Mach number and jet Mach number are 2.2 and 1.0, respectively in case of the pressure ratio p_0/p_b of 3.0. The height of the rods is hr/h^* = 0.8.

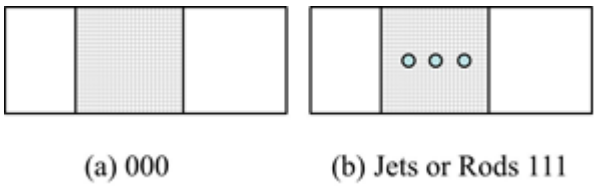

Fig. 4. Arrangements of jets or rods

Fig. 5. Thermal tuft probe

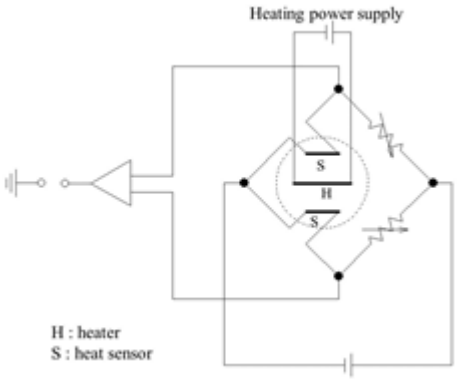

Fig. 6. Electronic circuit of Wheatstone bridge for heat sensors

3. Results and discussion

3.1. Shock positions and pressure distributions

Figures 7(a) through 7(c) show schlieren images at p_0/p_b = 2.1 for 000, Jet 111 and Rod 111, respectively. In Fig. 7(a), a starting shock wave is over the porous wall. Furthermore the incident shock wave on the lower wall is unclear due to the interaction between the starting shock wave and boundary layer developed by the porous cavity. A strong compression wave is observed at the upstream end of the cavity, which indicates the flow blowing from the cavity to the main duct flow. The boundary layer developed by the porous cavity and blowing reaches to the middle height of the duct and influences downstream flow. Figure 7(b) shows that a compression wave interacts with a bow shock wave created by the first jet. In addition to the pattern 000, the incident shock wave on the lower all for Jet 111 is not observed and a large boundary layer is visible. In Fig. 7(c), a starting shock wave, bow shock wave created by the first rod and compression wave from the upstream end of the porous wall are incident at the same point on the upper wall so they severely interact with each other. Because of the boundary layer, no incident shock wave on the lower wall can be observed. In all cases, the starting shock wave is located on the porous wall, and then the boundary layer grows, which causes the reduction of effective cross sectional area. As the results, the starting shock wave does not reach the lower wall.

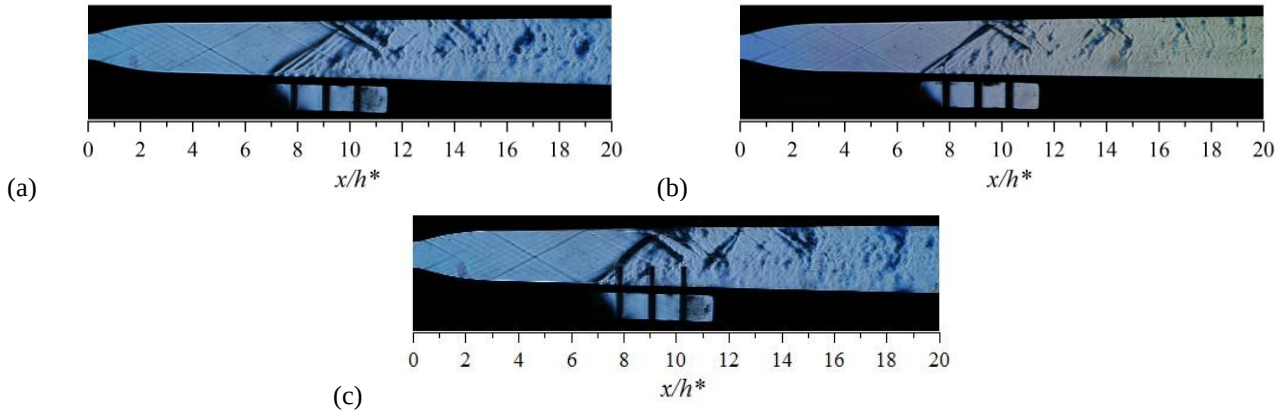

Fig. 7. Schlieren images at p_0/p_b=2.1 for (a) 000, (b) Jet111 and (c) Rod111.

Figure 8(a) through 8(c) show schlieren images at p_0/p_b = 3.0 for 000, Jet 111 and Rod 111, respectively. In Fig. 8(a), the starting shock wave exists at x/h^* = 14 on the upper wall and some weak compression waves are confirmed. In Fig. 8(b), three bow shock waves are created by the jets. First bow shock wave which is most upstream side is the strongest, and the next bow shock wave become weak as compared to first bow shock wave. On the contrary, the penetration height of the most downstream jet is the highest in all jets due to the wake of the two upstream jets. In Fig. 8(c), three clear bow shock waves as compared to Jet 111 are generated by the three rods. The dark line between x/h^* = 11 and 12 indicates that the bow shock wave impinging against the side wall. It was not created for pattern Jet 111, which is indicates that the bow shock wave created by the rod is wider than that of jet. But the first bow shock wave for Jet 111 is clearer than that of Rod 111. And there is the starting shock wave at x/h^*=15.5.

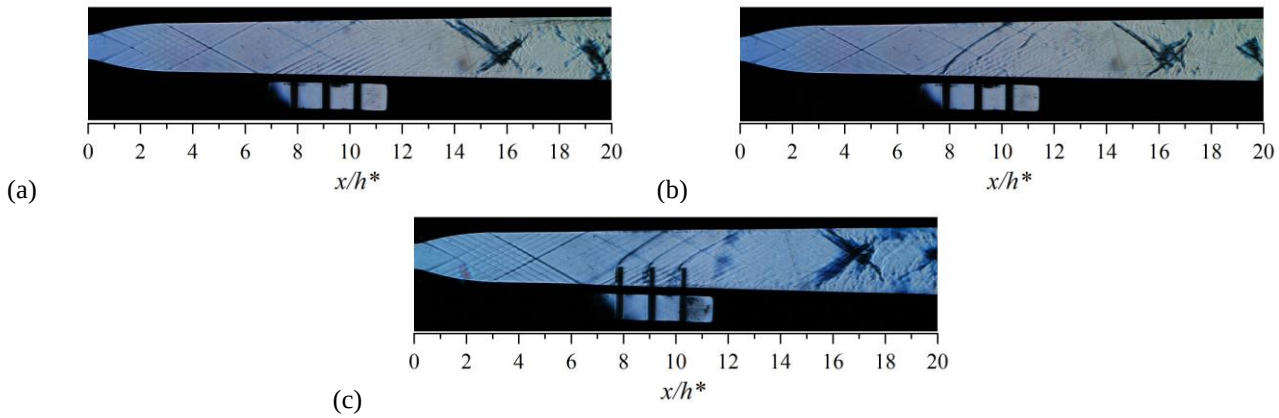

Fig. 8. Schlieren images at p_0/p_b=3.0 for (a) 000, (b) Jet111 and (c) Rod111.

Figure 9 shows the pressure distributions on the upper wall for pattern 000, Jet 111 and Rod 111, respectively. The peaks at x/h^* = 10.2 and 11.4 for Rod 111 and the peaks at x/h^* = 10.8 and 12 for Jet 111 are considered to be created by the bow shock waves. The first peak value for Jet 111 is larger than that of Rod 111. Jet 111 creates stronger bow shock wave than that of Rod 111, which is indicated by the schlieren as discussed above. It is very interesting that only pattern Rod 111 has expansion region between x/h^* = 13.2 and 15. It indicates that a strong suction takes place downstream of the third rod. So influence of rods on the main flow is very large.

Figure 10 shows the starting shock positions on the lower wall for pattern 000, Jet 111 and Rod 111, which is used to discuss the relation between the shock position and the porous region in the following discussions. Subscript S and L indicate shock condition and lower wall, respectively. In Fig. 10, the shock positions which have unclear incident shock wave on the lower wall are not described. This result shows that the starting shock wave for Jet 111 passes through the porous cavity at lower pressure ratio 2.2 compared to 000 and Rod 111. The reason why Jet 111 takes lowest pressure ratio to pass through the porous cavity is that three jets aligned streamwise play a role of the second throat in an internal flow. As the results, the three jets decrease the cross sectional area forming the second throat, which leads to sudden passage of a starting shock wave through the second throat due to small pressure increases. There is variation in the shock positions when the starting shock wave is around the cavity, but shock positions for all patterns comes to almost the same location $x_{S,L}/h^*$ = 15.5 for the pressure ratio of 3.0.

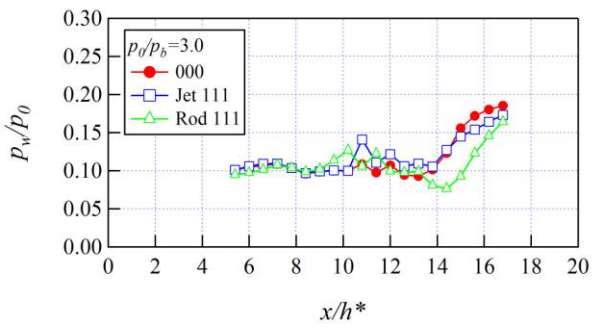

Fig. 9.Prressure distribution on upper wall

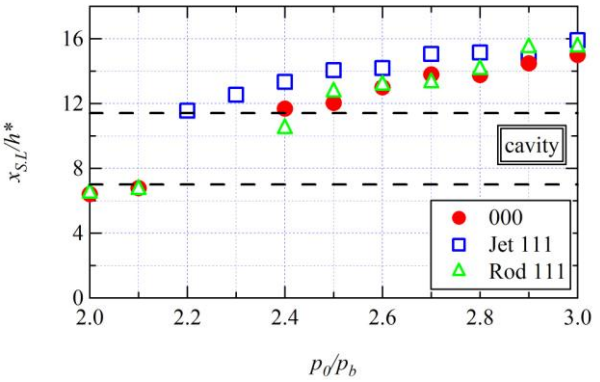

Fig. 10. Shock position

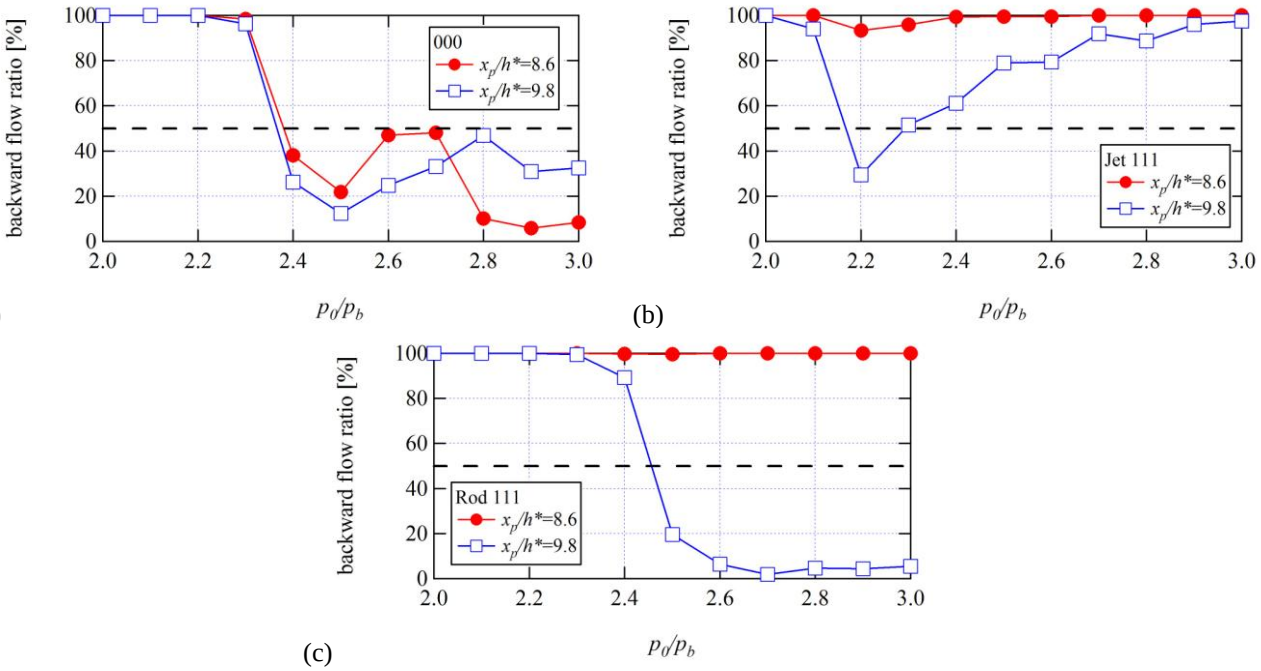

Fig. 11. Backward flow ratios for (a) Pattern 000, (b) Pattern Jet111 and (c) Pattern Rod111.

3.2. Backward flow ratio

Figures 11(a) through 11(c) show the backward flow ratios for the pattern 000, Jet 111 and Rod 111, respectively. The backward flow ratio is defined as a ratio of the time of backward flow to the total measurement time. In Fig. 11(a), the

backward flow ratios at $x_p/h^* = 8.6$ and 9.8 decreasing from $p_0/p_b = 2.4$ at which the starting shock passes through the porous region. After pressure ratio of 2.4, the backward flow ratio is below 50%, thus the flow direction in the cavity is forward to the main flow after the starting shock wave passing the porous wall. In Fig. 11(b), the backward flow ratio at $x_p/h^* = 9.8$ suddenly decrease at $p_0/p_b = 2.4$ and then it gradually increases to 100%. The pressure ratio of 2.2 is the pressure ratio of the starting shock wave passing over the cavity so the flow in the cavity is considered to be unstable. After the starting shock wave passes through the cavity, the flow in the cavity is stable because the backward flow ratios at each measurement position indicate 100% denoting the backward flow in the cavity all the time. Figure 10(c) shows that the backward flow ratio at $x_p/h^* = 9.8$ decreases at $p_0/p_b = 2.4$ and reaches nearly 0%. It indicates forward to the main flow direction at $x_p/h^* = 9.8$ for the range of pressure ratios of between 2.5 and 3.0. The result of Rod 111 differs from that of Jet 111. In our proposal concept of mixing enhancement, the result of Jet 111 is favorable because the backward flow ratio indicates that the flow direction in the cavity is opposite to the main flow except for the pressure ratio of 2.2 and 2.3.

4. Conclusions

The interaction between the high speed main flow and jets and rods surrounded by the porous cavity were investigated using the schlieren method, pressure measurement, and flow direction measurement in the cavity with a thermal tuft probe. The results are summarized as follows:

1. When the starting shock wave is over the porous cavity, the interaction between starting shock wave and boundary layer developed by the porous wall is occurs, which makes incident shock wave on the lower wall unclear.
2. Only Rod 111 has the expansion region on the upper wall downstream of the pressure increase due to the bow shock wave.
3. The starting shock wave for Jet 111 passes through the porous region at $p_0/p_b = 2.2$, which is the lowest pressure ratio in all cases.
4. Jet 111 is found to achieve the opposite direction to the main flow in the cavity, which is expected to occur with our proposed device. However, more detailed studies might be needed for the best combination and alignment of the jets.

References

[1] Rogers, R.C., Capriotti D.P., and Guy R.W., 1998. Experimental Supersonic Combustion Research at NASA Langley, AIAA Paper , 98－2506.
[2] Hanson, T. C. and Settles, G. S., 2003. Particle Temperature and Velocity Effects on the Porosity and Oxidation of an HVOF Corrosion-Control Coating, Journal of Thermal Spray Technology, Vol. 12, No. 3, pp. 403‐415.
[3]R. Honig, D. Theisen, R. Fink, R Lachner, G. Kappler, D. Rist, P. Andrsen, 1996. Experimental Investigation of a Scramjet Model Combustor with Injection through a Swept Ramp Using Laser-Induced Fluorescence with Tunable Excimer Lasers, Twenty-Sicth Symposium (International) on Combustion/The Combustion Institute, pp.2949-2956
[4] Ian A. Waitz, Frank E. Marble, Edward E. Zukoski, 1993. Investigation of a Contoured Wall Injector for Hypervelocity Mixing Augmentation, AIAA Journal Vol.31, No.6, pp. 1014 - 1021
[5] Barber, M.J., Schetz, J.A. and Roe, L.A., 1997. Normal, Sonic Helium Injection through a Wedge-Shaped Orifice into Supersonic Flow, Journal of Propulsion and Power Vol.13, No.2, pp.257-263
[6] M. Yaga, S. Tabata, P. Doerffer, K. Oyakawa, 2003. Numerical Simulation of Supersonic Mixing Enhancement with Porous Cavity, AIAA-Paper, 2003‐3461
[7]M. Yaga, K. Yamamoto, P. Doerffer, K. Oyakawa, 2006. Study of Interaction between Supersonic Flow and Rods Surrounded by Porous Cavity, Journal of Thermal Science Vo.15, No.4, 324-330
[8] C. P. Häggmark, A. A. Bakchinov, P. H. Alfredsson, 2000. Measurements with a flow direction boundary-layer probe in a two-dimensional laminar separation bubble, Experiments in Fluid 28, pp.236-242
[9] N. Kuniyoshi, M. Yaga, A. Koda, I. Teruya, M. Ishikawa, 2012. Experimental study of interaction between supersonic duct flow and jets surrounded by the porous cavity, Experimental Thermal and Fluid Science, Volume 40, pp185-194
.

Available online at www.sciencedirect.com

SciVerse ScienceDirect

Procedia Engineering 00 (2012) 000–000

Procedia Engineering

www.elsevier.com/locate/procedia

5th BSME International Conference on Thermal Engineering

Performance and Emission Comparison of a DI Diesel Engine Fueled by Diesel and Diesel-biodiesel Blend without and with EGR Condition

Md. Shazib Uddin*, S. M. Najmul Hoque and Murari Mohon Roy

Department of Mechanical Engineering, Rajshahi University of Engineering and Technology, Rajshahi-6204, Bangladesh

Abstract

This study investigates the performance and emissions of a direct injection (DI) diesel engine fuelled by neat diesel and B20 (blend of 20% biodiesel-80% diesel) under various load conditions and engine speeds without and with low percentage of exhaust gas recirculation (EGR). Here 10% EGR was attempted. Engine performance (brake thermal efficiency and brake specific fuel consumption), and the exhaust emissions (NOx and CO) were measured. The result showed that, the brake thermal efficiency (η_{th}) of B20 was almost similar or a slight lower, but brake specific fuel consumption (bsfc) was a little higher than neat diesel. At no load or low load conditions without EGR, carbon monoxide (CO) was higher and oxides of nitrogen (NOx) were lower with B20 than that of diesel. However, under high load conditions, NOx became higher and CO reduced significantly with B20. Application of EGR at these high load condition, diesel and B20 produced no change in thermal efficiency and bsfc in comparison to non-EGR. Furthermore, B20 showed higher reduction in NOx than diesel. Hence, B20 with 10% EGR can safely be used in diesel engine without any significant penalty in engine performance and with higher NOx reductions.

Keywords: DI diesel engine performance; emission; renewable alternative fuel; biodiesel; EGR

1. Introduction

The growing concern on environmental pollution caused by the extensive use of conventional fossil fuels has led to search for more environment friendly and renewable fuels. Biofuel such as alcohols and biodiesel have been proposed as alternatives for internal combustion engines [1-2]. In particular, biodiesel has received wide attention as a replacement for diesel fuel because it is biodegradable, nontoxic and can significantly reduce toxic emissions and overall life cycle emission of carbon dioxide (CO_2) from the engine when burned as a fuel [3]. Several countries including India have already begun substituting the conventional diesel by a certain amount of biodiesel [4]. The use of biodiesel is being promoted by EU countries to partly replace petroleum diesel fuel consumption in order to reduce greenhouse effect and dependency on foreign oil. Meeting the targets established by the European Parliament for 2010 and 2020 would lead to a biofuel market share of 5.75% and 10%, respectively [5].

* Corresponding author. Tel.: +8-801-717-548191; fax: +8-807-217-50319.
E-mail address: shazib0397@gmail.com

In near future, biodiesel fuels offer a potentially very interesting alternative regarding harmful emissions. Additionally, biodiesel does not contain any sulfur. Although biodiesel has many advantages, it still has several properties, needed to be improved, such as lower calorific value, lower effective engine power, higher emission of NOx, and greater sensitivity to low temperatures. Many investigations have shown that using biodiesel in diesel engines can reduce hydrocarbon (HC), CO and particulate matter (PM) emissions but NOx emission may increase [6]. The increase in NOx emission serves as biodiesel's major impediment to widespread use [7]. In order to reduce this adverse effect, investigations have been carried out on different approaches for reducing NOx emission when biodiesel is used. The increase in NOx emission can be avoided through modifying the properties of the biodiesel [7] or through adjusting engine setting [8]. Szybist et al. looked into the problem by considering the use of cetane improver for modifying ignition delay and the use of biodiesel with different bulk modulus for modifying fuel injection timing; both approaches have the potential for reducing NOx emission. Leung et al. concluded that controlling an individual engine operating parameter cannot acquire satisfactory results on optimizing engine emission; thus, multiparameter adjustment is required for reducing simultaneously HC, NOx and PM emissions [8]. Fernando et al. reviewed the NOx reduction methods for biodiesel fuels [9]. They concluded that the thermal NOx mechanism is the major contributor to NOx emission, thus NOx can be reduced through the application of water injection, water emulsified biodiesel, ignition timing retardation or exhaust gas recirculation which can lead to reduction in flame temperature. However most of these methods will normally lead to deterioration in engine performance as well.

It was reported that engine parameters have significant effect on performance and emissions of diesel engine when run with biodiesel and its blend with diesel [10]. Hence, a study was undertaken at Rajshahi University of Engineering and Technology (RUET), Bangladesh to gather information on behavior of diesel engine when operated with biodiesel and its blend with diesel at varying engine parameters. Engine tests were carried out at different engine speeds and loads without and with exhaust gas recirculation (EGR). A low percentage of EGR was attempted to reduce NOx emissions without deterioration in engine performance.

2. Experimental setup and measurement

A four-stroke single cylinder naturally aspirated direct injection (DI) diesel engine with specifications as in Table 1 was used in this experiment. All experimental data were taken after 30 minutes of engine start after which the exhaust line temperature was no further increased i.e. constant and there was almost no fluctuation of emissions. This condition of the engine is chosen because of the consistent data at this condition.

Table 1. Engine specifications

Engine type	4-stroke DI diesel engine
Number of cylinders	One
Bore × Stroke	80 × 110 mm
Swept volume	553 cc
Compression ratio	16.5:1
Rated power	4.476 kW@1800 rpm
Fuel injection timing	24^0 BTDC
Fuel injection pressure	14 MPa (900-1099 r/min)
	20 MPa (1100-2000 r/min)

All experimental data were taken at various engine speeds (low, medium and high) after engine warm-up. The diesel fuel used in this study was No. 2 diesel fuel with lower calorific value of 43000 kJ/kg and cetane number 50. Soybean oil was selected as a source of biodiesel and collected from local market in Bangladesh. Loads (low, medium and high) were measured by electric dynamometer. Corresponding to each data point, exhaust emissions and fuel consumption were measured for diesel and blend of 20%-80% biodiesel and diesel (B20). B20 was selected due to the reference engine given a better performance in previous biodiesel study [11]. A flue gas analyzer (IMR 1400) was used to measure CO and NOx of exhaust gases. Each measurement was repeated and checked to ensure the accuracy of data.

3. Results and discussion

3.1 Engine performance

After the engine reached the stabilized working condition for each test, fuel consumption, load and exhaust emissions were measured, from which bsfc, torque and efficiency were computed. The variations of these parameters with respect to torque are presented.

Brake thermal efficiency (η_{th}) and bsfc with diesel and B20 with and EGR are presented in Figure 1 at 600 rpm at various engine load conditions (Fig. 1.a is for non-EGR and 1.b for 10% EGR condition). It is seen from the figure that, brake thermal efficiency increased as the engine torque increased with B20 and neat diesel for both EGR and non EGR conditions. On the other hand, bsfc decreased with engine torque for B20 and neat diesel again for both EGR. Brake thermal efficiency with B20 was little lower than neat diesel due to higher bsfc of biodiesel but showed almost no variation with 10% EGR. At low load condition, thermal efficiency with B20 and neat diesel was only about 6%. At medium load, it was increased to about 10%, and at high load condition, it was about 17%. Brake specific fuel consumption with B20 was slight higher than neat diesel (about 1-2%) due to lower energy content of biodiesel. It decreased from about 1.5 kg/kW-hr to less than 0.5 kg/kW-hr, when engine torque was increased from 2.45 to 9.8 N-m.

The variation of brake thermal efficiency and bsfc with engine torque at 1000 rpm with and without EGR are illustrated in Figure 2. Brake thermal efficiency with B20 and neat diesel increased as the engine torque was increased for EGR and without EGR whereas bsfc decreased with B20 and neat diesel both without and with EGR condition as the engine torque increased**.**

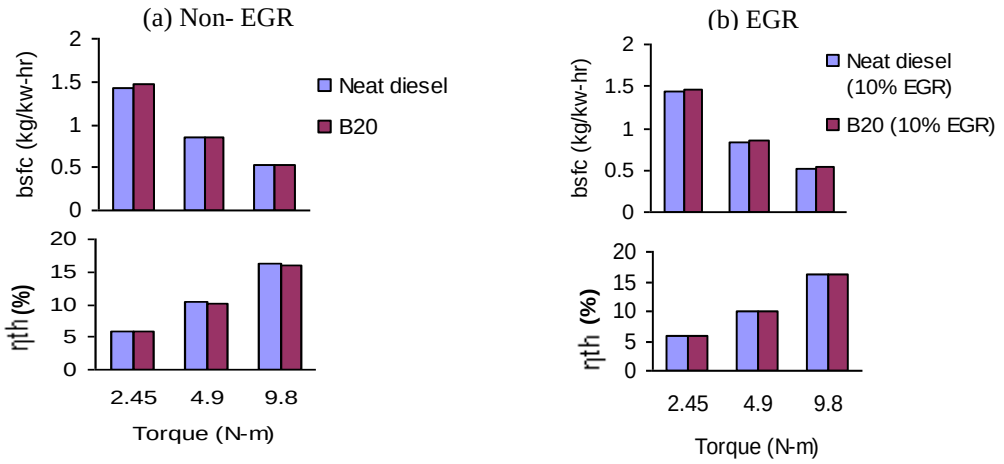

Fig. 1. Brake thermal efficiency and bsfc with diesel and B20 without and with EGR condition at 600 rpm

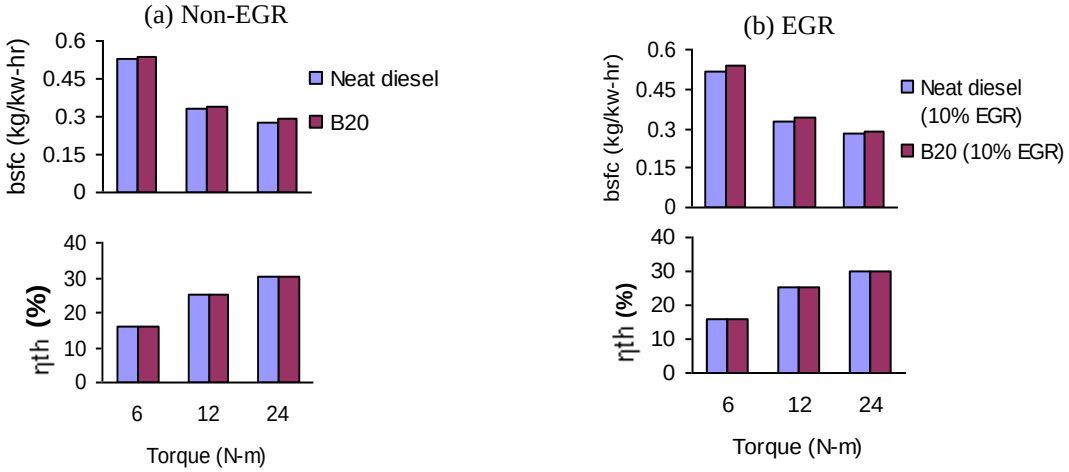

Fig. 2. Brake thermal efficiency and bsfc with diesel and B20 without and with EGR condition at 1000 rpm

Brake thermal efficiency with B20 without and with EGR condition was very similar to that with neat diesel for various loading conditions. The trend is similar to that described in Fig. 1. At low load condition, thermal efficiency with B20 and neat diesel without and with EGR condition was about 16%. At medium load condition, it was increased to about 26%, and at high load condition, about 30%. This was the highest thermal efficiency obtained in this study. Brake specific fuel consumption with B20 was a slight higher than neat diesel, about 1-3% without and with EGR condition. It decreased from about 0.54 kg/kW-hr to less than 0.3 kg/kW-hr, when engine torque was increased from 6 to 24 N-m.

Brake thermal efficiency and bsfc with diesel and B20 without and with 10% EGR at 1200 rpm for various engine loads are shown in Figure 3. Both brake thermal efficiency and bsfc with diesel and B20 were shown similar trend to that in Fig. 1 and 2. At low load condition, thermal efficiency with B20 and neat diesel was about 15%. It was increased to about 20%, at medium load condition and at high load condition; η_{th} was slightly less than 20%. Brake specific fuel consumption with B20 was always a little higher than neat diesel, about 2-4% without and with EGR condition. It decreased from about 0.59 kg/kW-hr to less than 0.4 kg/kW-hr, where engine torque was increased from 7.5 to 30 N-m.

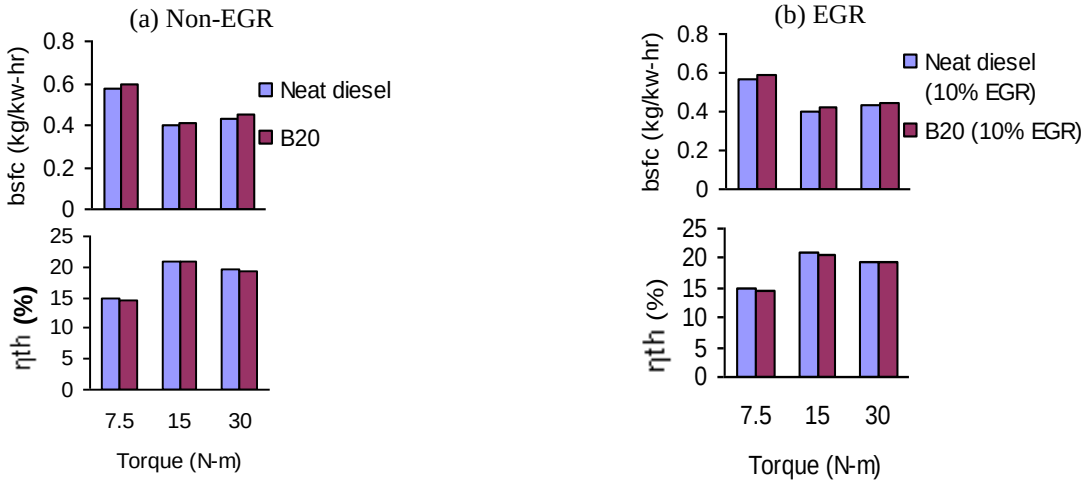

Fig. 3. Brake thermal efficiency and bsfc with diesel and B20 without and with EGR condition at 1200 rpm

3.2. Engine emissions

Variation of CO and NOx emissions with engine torque without and with EGR at 600 rpm are shown in figure 4 for neat diesel and B20. Fig. 4(a) is for non-EGR and 4(b) for 10% EGR condition. From the figure, it is seen that at no load or low load conditions CO emission with B20 is always higher than neat diesel without and with EGR. However, CO decreased with B20 and increased with neat diesel with increasing engine load.

Improved combustion as well as less CO was expected with biodiesel than diesel due to biodiesel's inherent O_2 content. However, at no or low load conditions, biodiesel showed poorer combustion and higher CO than diesel. Higher viscosity and boiling temperature of biodiesel as well as lower combustion temperature at low engine speed produced improper local mixture producing higher CO emission than diesel. The trend is reversed after a certain load. When the fuel-air equivalence ratio (φ) increases at higher engine loads, O_2 in biodiesel helps to produce less CO, whereas CO increases with diesel combustion. NOx emission for B20 and diesel is very similar if no EGR was employed. However, NOx reduction with EGR for B20 fuel was higher than diesel fuel.

Specific heat of biodiesel is higher than that of neat diesel. Therefore, higher amount of combustion heat is absorbed by the recirculated biodiesel exhaust lowering the combustion temperature. This helps to reduce higher NOx than diesel. Figure 5 illustrates the variation of CO and NOx emission with engine torque with and without EGR condition at 1000 rpm for diesel and B20. At no load condition, CO emission with B20 was higher than that of neat diesel without and with EGR condition. CO with B20 was decreased than that of neat diesel when engine load is increased. At higher engine speed of 1000 rpm, only no load condition produced poorer combustion with higher CO emission with B20 than neat diesel.

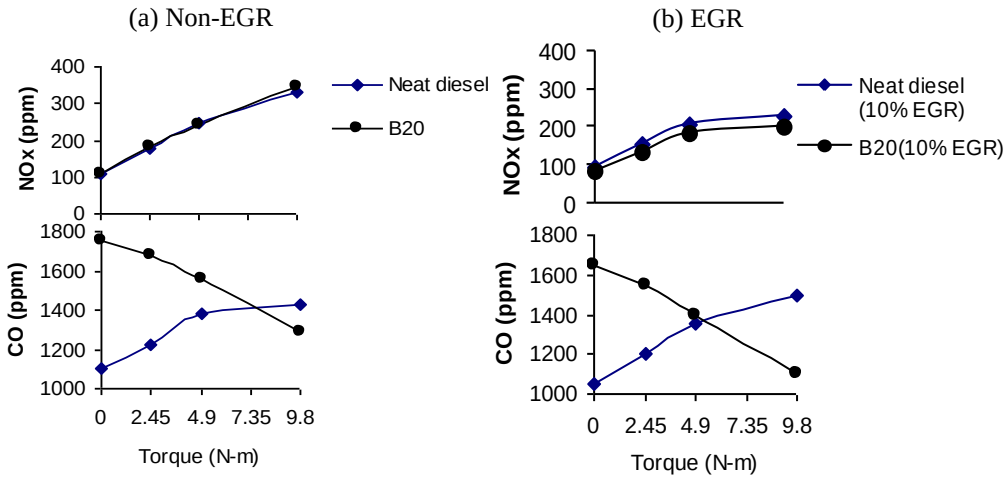

Fig. 4. CO and NOx emissions with diesel and B20 without and with EGR condition at 600 rpm

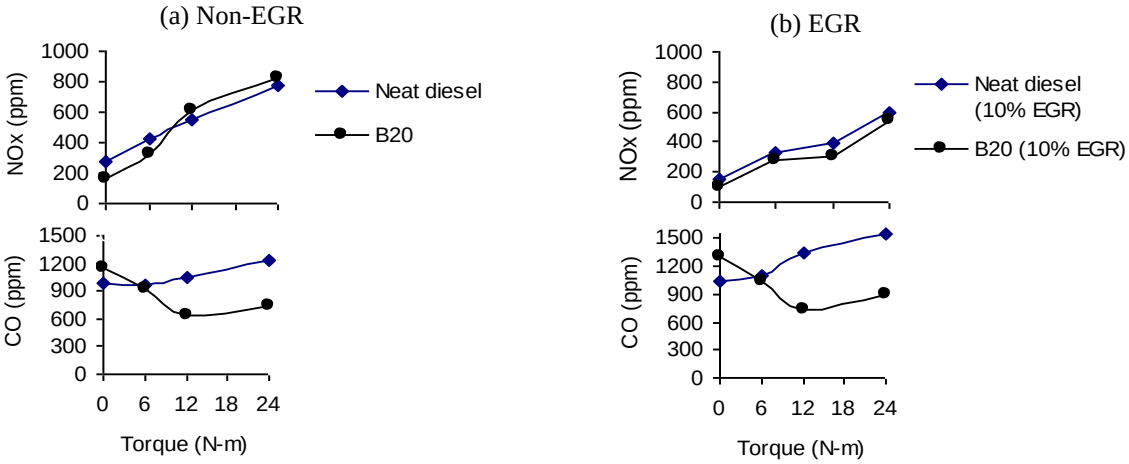

Fig. 5. CO and NOx emissions with diesel and B20 without and with EGR condition at 1000 rpm.

Without EGR, NOx emission with B20 at lower load condition was lower and it was higher than that of neat diesel at higher load . However, with EGR, B20 always produced lower NOx than that of neat diesel similar to that in Fig. 4.

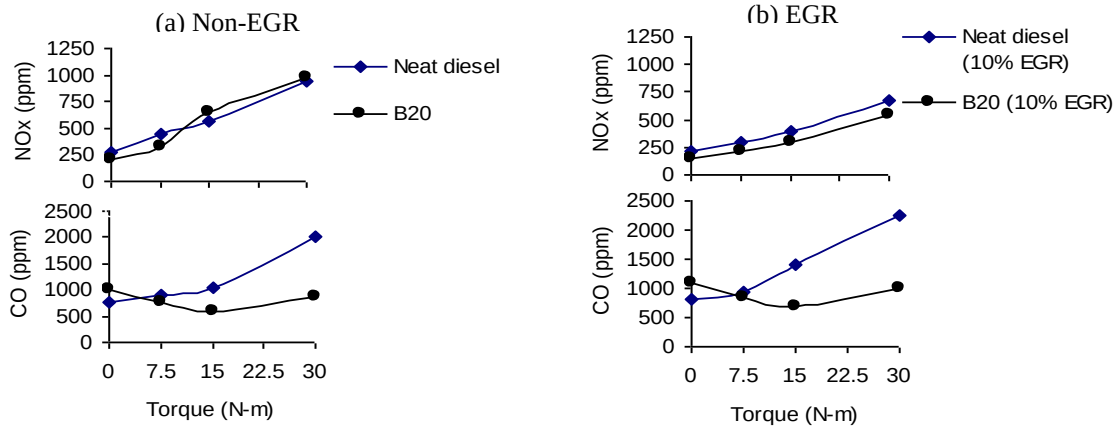

Fig. 6. CO and NOx emissions with diesel and B20 without and with EGR condition at 1200 rpm

The variation of CO and NOx emission with engine torque without and with EGR condition at 1200 rpm are demonstrated by Figure 6. At no load condition, CO emission for B20 was slightly higher than that of neat diesel, and with increasing load CO was always lower than diesel fuel without and with EGR. Here also NOx reduction for B20 is higher than neat diesel fuel. From experimental results it was understood that biodiesel combustion at low temperature condition deteriorates combustion quality and produces higher CO without or with low percentage of EGR due to higher viscosity of biodiesel and improper mixture formation. With EGR operation biodiesel reduced higher NOx than diesel due to higher specific heat of biodiesel exhaust, for which recirculated exhaust gas at EGR absorb higher amount of combustion heat.

4. Conclusions

The following conclusions can be drawn from the investigation.

- B20 showed similar thermal efficiency to that of the level of diesel with and with 10% EGR.
- The bsfc of B20 was about 1-4% higher than that of diesel for both EGR and without EGR conditions.
- At no load or low load conditions, B20 produced higher CO than diesel, but at high load condition B20 produced significantly lower CO than diesel with or without EGR condition.
- At no load or low load condition without EGR, B20 produced lower NOx than the neat diesel, but at higher load condition NOx emission with B20 was higher than neat diesel. With 10% EGR, B20 always produced lower NOx than that of diesel at all the engine speed and load.

References

[1] Agarwal, AK., 2007. Biofuels (alcohols and biodiesel) applications as fuels for internal combustion engines, Prog Energ Combust Sci 33, p. 233–71.
[2] Demirbas, A., 2007. Progress and recent trends in biofuel, Prog Energ Combust Sci, 33, p. 1–18.
[3] Cvengros, J., Povazanec, F., 1996. Production and treatment of rapeseed oil methyl esters as alternative fuels for diesel engines, Bioresour Technol, 55, p. 145–52.
[4] Raheman, H., Ghadge, S.V., 2008. Performance of diesel engine with biodiesel at varying compression ratio and ignition timing, Fuel 87, p. 2659–2666.
[5] Magín, L., José, M. H., Lisbeth, L.L., Reyes G.C.Y.B., 2008. Effect of the alcohol type used in the production of waste cooking oil biodiesel on diesel performance and emissions, Fuel, vol. 87, p. 3161–3169.
[6] Sharp, C.A., Howell, S.A., Jobe, J., 2000. The effect of biodiesel fuels on transient emissions from modern diesel engines-part I: regulated emissions and performance, SAE Tech Pap Ser, No. 2000-01-1967.
[7] Szybist, J., Simmons, J., Druckenmiller, M., Al-Qurashi, K., Boehman, A., Scaroni, A., 2003. Potential methods for NOx reduction from biodiesel, SAE Tech Pap Ser, No. 2003-01-3205.
[8] Leung, D.Y.C., Luo, Y., Chan, T.L., 2006. Optimization of exhaust emissions of a diesel engine fuelled with biodiesel, Energ Fuel, 20, p. 1015–23.
[9] Fernando, S., Hall, C., Jha, S., 2006. NOx reduction from biodiesel fuels, Energ Fuel, 20, p. 376–82.
[10] Pandey, K.C., 2005. Investigations on use of soybean oil as a substitute fuel for diesel engines, Unpublished PhD thesis, IIT Kharagpur, India.
[11] Hoque, S.M. N., Uddin, M. S., Nabi, M. N., Rahman, M. M., 2008. "Biodiesel from Non-Edible Renewable Karamja Seed Oil and its Effect on DI Diesel Engine Combustion", Proceedings in the 4th BSME-ASME International Conference on Thermal Engineering, 27-29 December, Dhaka, Bangladesh

Available online at www.sciencedirect.com

SciVerse ScienceDirect

Procedia Engineering 00 (2012) 000–000

Procedia Engineering

www.elsevier.com/locate/procedia

5th BSME International Conference on Thermal Engineering

Study of effect of coating of piston on the performance of a Diesel Engine

K.Veerabhadrappa[a], R. Suresh Kumar[a]*, CS Ramesh[b]

[a]*Assistant Professor, Department of Mechanical Department, BMSCE, Baangalore & Research Scholaar, JNTU, Hyderabad*
[b]*Professor, Department of Mechanical Department, PESIT, Baangalore*

Abstract

Insulation of pistons in engines is aimed at reducing the heat losses and thus increasing the indicated efficiency. Thermal barrier coatings (TBCs) were used to simulate adiabatic engines with the intention not only for reduced in-cylinder heat rejection and thermal fatigue protection of underlying metallic surfaces, but also for possible reduction of engine emissions. The application of TBCs reduces the heat transfer to the engine cooling jacket through the combustion chamber surfaces (which include the cylinder head, liner, and piston crown) and piston rings. The insulation of the combustion chamber with this coating, which is mainly ceramic based, influences the combustion process and hence the performance and exhaust emissions characteristics of the engines. In the scenario of fast rising oil prices, insulation technologies are gaining importance as they help in saving fuel. A plasma sprayed thermal barrier coating of Titania was deposited on top of a piston for a Diesel engine and its effect on the engine performance is studied. Thermal stresses are analyzed using finite element analysis.

Keywords: Piston, Coating, Engine Performance, Finite Element Model, Thermal Stresses

1. Introduction

The thermal efficiency of IC engines can be increased by improving the combustion process and reducing loss of heat energy through the exhaust gases by applying thermal barrier coatings on the piston crown. This also helps to reduce specific fuel consumption and emissions. Atmospheric plasma spraying technique is used to apply the ceramic coatings as the method is versatile and can be used to apply wide variety of coatings on a spectrum of substrates and homogenous coatings can be formed. Besides, fast rise of the oil prices tends to attract insulation of combustion chamber with TBCs to reduce fuel consumption. For best efficiency, the combustion chamber has to be fully insulated to keep the process closer to adiabatic.

Piston crowns were coated with a layer of ceramic, which consisted of yttria-stabilized zirconia (YSZ) and measurement and comparison of engine performance, in particular fuel consumption, were made before and after the application of YSZ coatings deposited onto the piston crowns by S.H. Chan and K.A. Khor [S.H. Chan and K.A. Khor, 2000] and achieved fuel economy up to 6% at low engine power. Tests were performed on a single cylinder, four stroke, direct injection, diesel engine by P. N. Shrirao and A. N. Pawar whose piston crown, cylinder head and valves were coated with a 0.5 mm thickness of $3Al2O_3$ $.2SiO_2$ (mullite) over a 150 µm thickness of NiCrAlY bond coat and showed that there was 2.18% decreasing on specific fuel consumption, as much as 12% increase in exhaust gas temperature , as much as 20.64% increase in NOx emission of exhaust gas, 22.05% decrease in CO emission of exhaust gas and 28.20% decrease in on HC emission of exhaust gas of LHR engine with turbocharger compared to standard engine at full load [P. N. Shrirao and A. N. Pawar, 2011]. Engine components were coated with ZrO_2 /Al_2O_3 using PSC technique by A.P. Sathiyagnanam, C.G. Saravanan and S. Dhandapani for a thickness of 150 microns and the results indicated reduction in fuel consumption, NOx emission and

* Corresponding author. Tel.: 9739097890; fax: +91-80- 26614357.
E-mail address: rupanagudisureshkumar@yahoo.co.in

slight increase in thermal efficiency of the engine [A.P. Sathiyagnanam et al, 2010]. Vijaya Kumar K.R and Sundareswaran V. in their study on the effect of thermal barrier coatings on Diesel engine performance of PZT loaded Cyanate Modified Epoxy coated combustion chamber applied the coating made up of 20% Lead Zirconate Titanate (PZT) in 60% Cyanate modified Epoxy system to the combustion chamber and showed that specific fuel consumption reduced by 15.89 % [Vijaya Kumar K.R and Sundareswaran V.,2011]. Tests were performed by Ekrem Bykkaya et al on a six cylinder, direct injection, turbocharged Diesel engine whose pistons were coated with a 350 µm thickness of $MgZrO_3$ over a 150 µm thickness of NiCrAl bond coat and found that there is 1–8% reduction in brake specific fuel consumption [Ekrem Bykkaya et al, 2006].

In this work, since the piston contributes mainly to heat loss and is the hottest part, piston is chosen for coating. Since Titanium dioxide is a very hard ceramic and forms a good TBC to be coated on piston, a bond coat of Ni was coated and 100 micron top coat of TiO_2 was applied on the piston to reduce thermal mismatch.

2. The coating process

Fig.1 shows Kirloskar AV1 Diesel engine piston was coated with Titanium Dioxide using Atmospheric plasma spray coating method. Trichloroethylene was used to clean the crown and remove all dust particles. 24 mesh Al_2O_3 was used to grit blast the crown to create rough surface so that the mechanical bond between coating and substrate remains strong. To provide good bonding for the coating material on base metal, a bond coat Nickel was applied. Then TiO_2 powder was sprayed using a gun with a standoff distance of about 10 cm onto the piston crown to a thickness of 100 microns. Hydrogen and argon gases were used as inert gases and current and voltage were maintained at 495 amps and 70 volts respectively during the coating process.

Fig.1. AV1 Diesel engine piston coated with Titanium dioxide

3. Experimental set up

Table1: Engine Specifications

Engine type	**Kirloskar AV1, DI**
Stroke number	4
Cylinder number	1
Bore	80mm
Stroke length	110mm
Compression ratio	16.5 : 1
Maximum engine power	3.7 KW
Maximum engine speed	1500 rpm
Specific fuel consumption	245 g/Kwh

Fig.2(a) and (b) show four stroke diesel engine, Kirloskar AV1 type, water cooled and single cylinder engine is to be used for the investigation of engine parameters with coated piston before and after running the engine respectively. Table 1 gives the specifications of the engine.

Fig. 2. (a) Coated piston before engine is run (b) Coated piston after engine is run.

4. Experimental Procedure

The engine was maintained at 1500 rpm with uncoated and coated piston. The fixed injection pressure of 200 bar was maintained. The performance test was conducted on the engine with uncoated and coated piston at different loads and at constant speed. The experiments were conducted at four loads 2, 4, 6 and 10 kg. The following observations were made and the parameters such as brake specific fuel consumption, brake thermal and indicated thermal efficiencies, mechanical efficiency, brake specific energy consumption , Air fuel ratio and Exhaust gas temperature were obtained. The variations of these parameters except exhaust gas temperature were plotted with respect to Brake Power and variation of exhaust gas temperature was plotted with respect to load.

5. Results and Discussions

5.1. Brake Specific fuel consumption

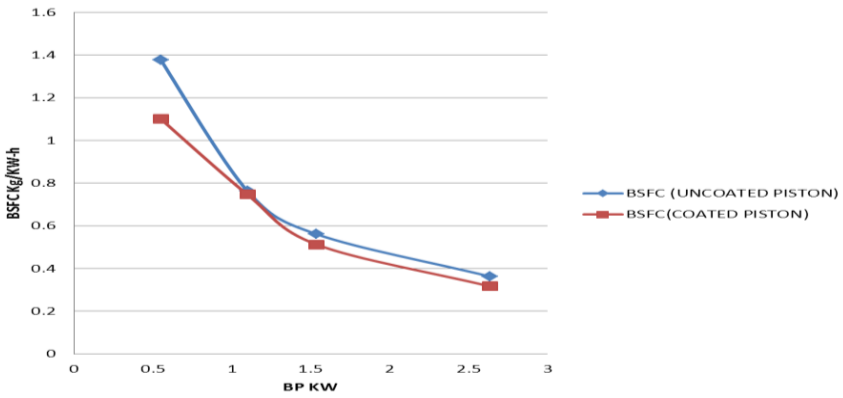

Figure 3: Comparison of brake specific fuel consumption and brake power of coated and uncoated piston

Fig.3 shows the comparison of the specific fuel consumption. In case of coated piston, specific fuel consumption of is less than the engine with uncoated piston. The decrease in the fuel consumption shows that the combustion of fuel is more efficient in case of engine run with coated piston.

5.2 Brake Thermal Efficiency

Fig.4 shows the comparison in the brake thermal efficiency of the engine with uncoated and coated piston. It shows that there is an increase in the brake thermal efficiency of the engine with coated piston compared to the uncoated piston. There

is almost 3% increase in the brake thermal efficiency of the engine run with coated piston.

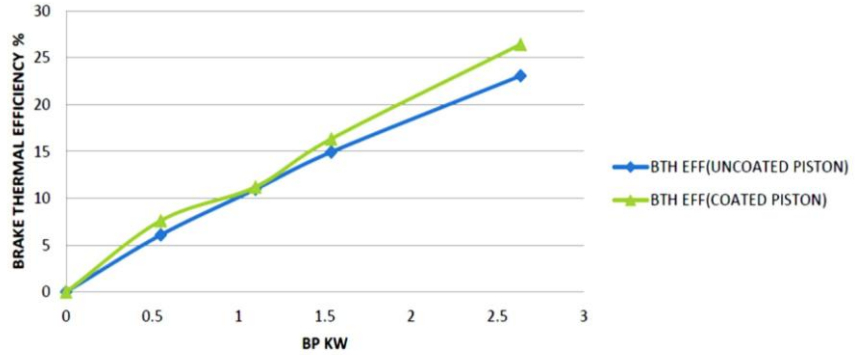

Fig.4. Comparison of brake thermal efficiency vs brake power of the uncoated and coated piston

5.3 Indicated Thermal Efficiency

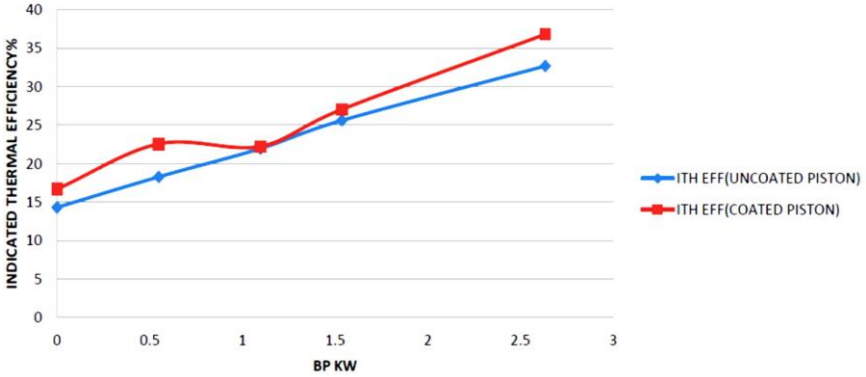

Fig.5. Comparison of indicated thermal efficiency vs brake power of the uncoated and coated piston

Fig.5 shows the comparison of indicated thermal efficiency. It shows that there is increase in the Indicated thermal efficiency of the engine with coated piston compared to that of the uncoated piston. There is about 3% increase in the thermal efficiency of the engine run with coated piston.

5.4 Mechanical Efficiency

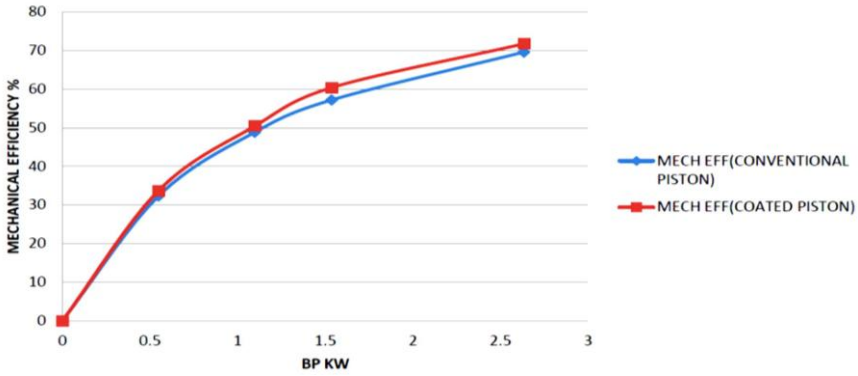

Fig.6. Comparison of mechanical efficiency vs brake power of the engine with uncoated and coated piston

Fig.6 shows the comparison of mechanical efficiency of engine with uncoated and coated piston. It shows that

there is an increase in the brake mechanical efficiency of the engine with coated piston compared to that of the uncoated piston. There is about 2% increase in the mechanical efficiency of the engine run with coated piston.

5.5 Brake Specific Energy Consumption

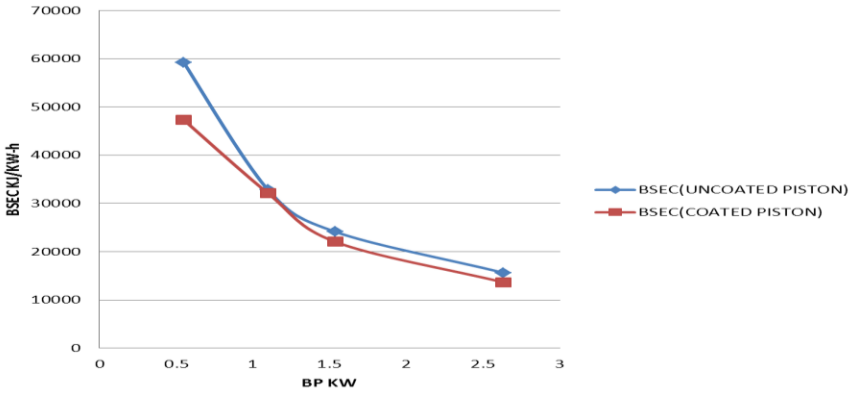

Figure 5.7: Comparison of brake specific energy consumption with brake power for engine with coated and uncoated piston.

Fig. 5.7 shows the comparison of brake specific energy consumption with brake power for engine with uncoated and coated piston. It was found that the brake specific energy consumption in diesel engine with coated piston was comparatively lesser as compared to engine with uncoated piston as the specific fuel consumption is lesser in the case of engine with coated piston.

5.6 Air Fuel Ratio

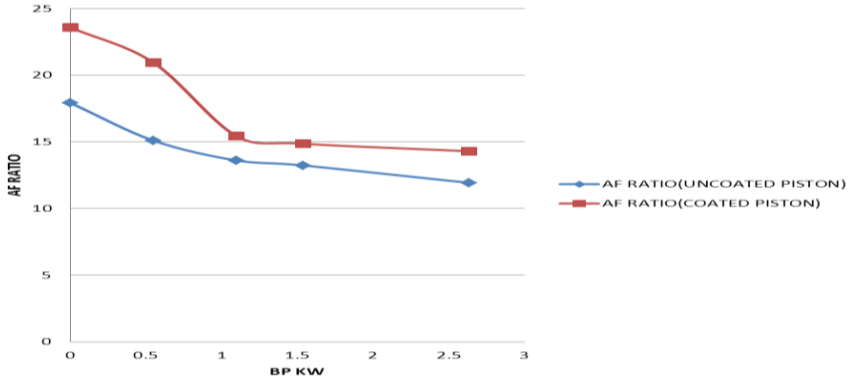

Figure 5.8: Comparison of air fuel ratio with brake power for diesel engine with coated piston and uncoated piston.

Fig.5.8 shows the comparison of air-fuel ratio with brake power for diesel engine with uncoated and coated piston. As the fuel consumption is more in the case of engine with uncoated piston, the air-fuel ratio for coated piston is comparatively more as compared with that of the engine with uncoated piston.

5.7 Exhaust Gas Temperature

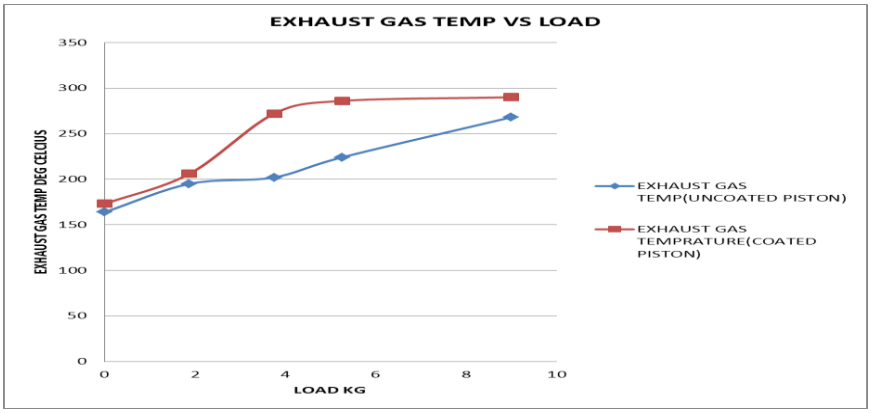

Fig5.9: comparison of exhaust gas temperature with load for diesel engine with coated and uncoated piston.

Fig.5.9 shows the comparison of exhaust gas temperature for diesel engine with coated and uncoated piston. There was a substantial increase in the exhaust gas temperature for the engine with coated piston as the piston crown is insulated and most of the heat produced is contained inside the combustion chamber thereby increasing exhaust gas temperature. The exhaust temperature for engine with coated piston was about 40^{o}C in excess as compared to the standard engine

6. Conclusions

From the experimentation, the following conclusions were drawn.

1. Normal engine is modified by insulating the piston crown with Titanium dioxide coating using plasma spraying technology.

2. The fuel consumption in case of coated piston is less than the engine with uncoated piston.

3. There is about 3% increase in the brake thermal efficiency of the engine run with coated piston as compared with standard diesel engine.

4. There was about 2% increase in mechanical efficiency

5. It was found that the brake specific energy consumption in diesel engine with coated piston was comparatively lesser as compared to engine with uncoated piston.

6. There was a substantial increase in the exhaust gas temperature for the engine with coated piston as compared to normal diesel engine with exhaust temperature about 40 degree Celsius excess than standard engine.

References

[1] S.H. Chan , K.A. Khor. The Effect of Thermal Barrier Coated Piston Crown on Engine Characteristics. JMEPEG (2000) 9:103-109
[2] P. N. Shrirao, A. N. Pawar. Evaluation of Performance and Emission characteristics of Turbocharged Diesel Engine with Mullite as Thermal Barrier Coating. International Journal of Engineering and Technology Vol.3 (3), 2011, 256-262.
[3] A.P. Sathiyagnanam, C.G. Saravanan ,S. Dhandapani. Effect of Thermal-Barrier Coating plus Fuel Additive for Reducing Emission from Di Diesel Engine. Proceedings of the World Congress on Engineering 2010 Vol II
[4] Vijaya Kumar K.R, Sundareswaran V. The Effect of Thermal Barrier Coatings on Diesel Engine Performance of PZT Loaded Cyanate Modified Epoxy Coated Combustion Chamber. Jordan Journal of Mechanical and Industrial Engineering, Volume 5, Number 5, Oct. 2011, ISSN 1995-6665, Pages 403 – 406
[5] Ekrem Bykkaya, Tahsin Engin and Muhammet Cerit. Effects of thermal barrier coating on gas emissions and performance of a LHR engine with different injection timings and valve adjustments. Energy Conversion and Management 47 (2006) 1298–1310